POLITECNICO DI MILANO

SCUOLA INTERPOLITECNICA DI DOTTORATO

Doctoral Program in Bioengineering

Final Dissertation

Multimodal sensors management in Computer and Robot Assisted Surgery

Alberto Vaccarella

Tutor
prof. Giancarlo Ferrigno

Supervisor
Elena De Momi, PhD

Co-ordinator of the Research Doctorate Course
prof. Maria Gabriella Signorini

28th February 2013

Abstract

Technological advancements and research efforts in biomedical engineering over the last three decades, led to the development of Computer Assisted Surgery (CAS) systems. CAS systems facilitate complex surgical procedures with technologies and methods to assist the surgeon from the preoperative planning phase to the intra-operative phase, providing image guidance and, in some cases, robotic assistance. Among the different technologies adopted in CAS, position sensing devices play a central role for surgical navigation, providing intra-operative localization of patient and surgical instruments. Moreover, other types of sensors have been recently introduced in CAS systems, such as intra-operative imaging devices (mainly ultrasound, but also expensive intra-operative MRI or CT systems) and force sensors. The need for integration and consistent management of such technologies has recently arisen.

In this thesis we studied and developed a software architecture for multimodal sensors management in the operating room (OR) and data fusion to overcome limitations of currently available technology. In more detail, our work focused on a software architecture to acquire data from position sensors (optical and electromagnetic) and intra-operative ultrasound imaging device in a consistent manner, both in time and space. In fact, different sensors need to be correctly aligned in time (different clocks, different acquisition rates) but also in space since each sensor has its own reference frame. Moreover, based on the developed architecture, we designed and tested a sensor fusion algorithm to merge data from an optical and an electromagnetic localizer, to overcome their main limitations: line-of-sight occlusions and electromagnetic field distortions respectively.

The *Sensor Manager* framework was tested and validated in a real OR as part of a complex system for computer and robot assisted neurosurgery within the ROBOCAST project (EU grant FP7-ICT 2007-215190). The sensor fusion algorithm proved to compensate optical line-of-sight occlusions with errors

below 1 mm, which satisfies demanding requirements of neurosurgical procedures. Furthermore, the sensor fusion increased the robustness to electromagnetic field disturbances, reaching, in condition of high distortion, errors comparable with the nominal accuracy of an electromagnetic localizer in a metal-free environment.

The developed system represents a step towards the vision of the *OR of the future*, which envisages a smart environment with a context-aware sensory system capable of understanding human commands and even intentions for a seamless human-machine interaction and adaptive surgical workflow management.

Acknowledgements

Where you probably start reading I finish writing, and of course I conclude this long journey thanking all the people that helped me along the way.

First of all I thank my family for having shared my decisions and for having supported me in the hard times that occurred in the last three years.

I would not be here without the help of my supervisors to whom I am grateful. Thanks to Giancarlo who taught me that I must always find a way to break what I create if I want to rebuild it better; his curiosity has been an example for me. Thanks to Elena who injected her enthusiasm for research into me and taught me to work under pressure, to meet deadlines, to try and do things even when I am not sure I measure up. Thanks to Andinet, my supervisor during my internship at Kitware, who picked me up at the airport when I first arrived in Raleigh and stayed by my side in the office and outside the work for my entire stay in the U.S.

Thanks to my lab mates, for sharing with me what they know and more importantly their questions, and of course for all the funny moments: the "burratina Monday", the "Kebab Tuesday", the "Chicken Frieday". Well, no, we do not only eat, we also drink (beers) and play sports, uhm…actually it's basically darts but still…

Thanks to all my friends, many of them now work abroad but all of them I feel close to me every day.

to my family

Contents

1 Introduction 1

1.1 Computer Assisted Surgery 1

1.2 Navigation systems 2

1.3 Sensors Classification and Surgical applications 4

1.4 Open issues 8

2 Data acquisition framework: the "Sensor Manager" 11

2.1 Background 11

2.2 The CAS system 13

2.3 The Sensor Manager 15

2.4 The experimental protocol 17

2.4.1 Experiment #1 17

2.4.2 Experiment #2 19

2.5 Results 19

2.5.1 Experiment #1 19

2.5.2 Experiment #2 20

2.6 Use case: 3D Ultrasound temporal calibration 21

2.7 Discussion 23

3 Sensor fusion 27

3.1 Multi-sensor data fusion 27

3.2 The Unscented Kalman Filter 31

3.3 UKF-based sensor fusion for robust tracking in surgical navigation 33

3.3.1 Background 33

3.3.2 Materials and methods 36

3.3.3 Results 49

3.3.4 Discussion 55

4 Conclusions **59**
Appendix A **64**
Bibliography **74**

Acronyms

ACE Adaptive Communication Environment

ACTIVE Active Constraints Technologies for Ill-defined or Volatile Environments

CAS Computer Assisted Surgery

CORBA Common Object Request Broker Architecture

DRF Dynamic Reference Frame

EKF Extended Kalman Filter

EMDRF Electromagnetic Dynamic Reference Frame

EMTS Electromagnetic Tracking System

IGSTK Image-Guided Surgery Toolkit

KF Kalman Filter

ODRF Optical Dynamic Reference Frame

OTS Optical Tracking System

TAO The ACE Orb

RF Reference Frame

ROBOCAST ROBOt and sensors integration for Computer Assisted Surgery and Therapy

SF Sensor Fusion

UKF Unscented Kalman Filter

UT Unscented Transform

Chapter 1

Introduction

1.1. Computer Assisted Surgery

Surgical interventions are among the most challenging activities performed by humans. They require years of training and education, coupled with practice, intuition, and cognitive as well as manual abilities.

To facilitate such a complex task, research efforts in biomedical engineering led to the introduction of Computer Assisted Surgery (CAS). CAS is a set of technologies and methods to assist the surgeon from the preoperative planning phase to the intra-operative phase, providing image guidance and, in some cases, robotic assistance to perform the procedure. Although CAS is a relatively young concept dating back to the end of the 80's, many of the underlying concepts have been developed and refined over the last century.

The first example of using an external device to define a space within an anatomical structure and to guide a tool within that space, was the so-called stereotactic frame by Horsley and Clark (1908). The frame was meant to be fixed to a subject's head (in this case, monkeys) and to be aligned with external anatomical landmarks (e.g. auditory canals) with the purpose of guiding electrodes insertion. The fundamental assumption of this approach was that the brain has a constant structure and that external landmarks could be used to predict internal structures.

Only half a century later, with the advancement of imaging techniques, Horsley and Clark concept was renewed first by Spiegel et al. (1947) so that two orthogonal images (anterior-posterior and side-to-side) could be made with the frame mounted on the head. Identifying the same feature in both the images allowed to resolve the third dimension and opened the way for

human stereotaxy. In the next years a number of stereotactic frames were designed (Leksell, 1951) (Talairach, 1957) (Todd, 1967).

A milestone that dramatically changed the history of image guided surgery is the invention of computed tomography (CT) in 1973 (Hounsfield, 1973). The introduction of this technology and the concept of a three-dimensional voxel rather than a two-dimensional pixel, highly increased the targeting accuracy: the third dimension is, in fact, embedded in the imaging technique, avoiding the process of feature identification on two orthogonal plane images (as in Spiegel's frame). Later on, the introduction of magnetic resonance imaging (MRI) and of personal computers, allowed putting the basis for current concept of image-guided surgery. In particular, this happened when in the mid-80's researchers perspective changed. The idea of localizing the target on the images and then moving to physical space was reversed and gave birth to the so-called *frameless stereotaxy*: the attention was moved to the intra-operative position of the surgical instrument that is then displayed onto the pre-operative images (Roberts et al., 1986) (Friets et al., 1989).

Although stereotaxy arose in the field of neurosurgery, technological advancements in the past 20 years have modified the concept of modern operating rooms (ORs) with a broader and broader introduction of CAS systems, which promise to enhance the outcome, safety and standardization of different types of surgical procedures (Joskowicz and Taylor, 2001) (Taylor and Kazanzides, 2008).

Technology in modern ORs is usually classified as passive or active (DiGioia et al., 2004); the first refers to surgical navigation systems, the latter includes robotic systems.

1.2 Navigation systems

The general task of surgical navigation can be subdivided in five smaller sub-processes:

1. Preoperative data acquisition, usually CT and/or MRI images
2. Localization and tracking of the position of the surgical tool or therapeutic device

3. Registration of the localizer volume with the preoperative data
4. Visualization of the position of the tool with regard to medically important structure visible in the preoperative data
5. Evaluation of differences between the preoperative data and the intra-operative reality

To this extent, navigation platforms include the following hardware:

- a localization system for tracking the position and orientation of patient body parts and surgical instruments;
- a computer for managing the data acquisition stream and for registering the data to preoperative images, typically Magnetic Resonance Imaging (MRI) or Computed Tomography (CT) scans;
- a display for visualization
- optionally, intra-operative imaging device (intra-operative US imaging, or more complex and expensive intra-operative CT and MRI imaging devices) can be used to evaluate the difference with the preoperative plan, in particular in case soft tissues are involved

Nowadays, surgical navigation systems find application in various fields such as orthopedic surgery (Sugano, 2003), (Hananouchi et al., 2009), abdominal surgery (Zhang et al., 2006), ENT surgery (Klimek, 2005) and neurosurgery (Willems et al., 2006).The use of navigation systems in orthopedic procedures, such as total knee arthroplasty or hip resurfacing, proved to enhance mechanical axis alignment, accuracy and precision prosthesis positioning, to shorten the recovery period for patients and to reduce the length of the learning curve for young surgeons (Bathis et al., 2004) (Seyler et al., 2008). Abdominal surgery, both open and percutaneous procedures, also exploit navigation systems to improve intra-operative orientation during biopsies and tumor resections and to augment information displayed to surgeons in standard image-guided procedures (typically CT-guided or ultrasound-guided percutaneous surgery) (Beller et al., 2007) (Lange et al., 2004) (Das et al., 2006). Navigation systems proved to help surgeons during ENT surgery in localizing complex structure in the frontal and maxillary sinus (Gunkel et al., 2009), (Strauss et al., 2009).

Navigation systems in neurosurgery pioneered the advent of this technology in other types of surgeries, due to their tight relationship with stereotaxy first and image-guidance later. Nowadays navigation systems are used in several neurosurgical procedures, in particular for stereotactic procedures like the insertion of electrodes for deep brain stimulation (Guo et al., 2006), brain biopsies or deep tumor removal (Tanaka et al., 2009).

1.3 Sensors Classification and Surgical applications

In CAS, different types of sensors, which can be classified as follows according to the information provided to the surgeon, are widely used:

1. Position information-sensing devices.
2. Force-sensing devices.
3. Intra-operative imaging devices.

Depending on their working principle, each of the previous classes can be further subdivided. Position information-sensing devices can be mechanical, ultrasonic, optical, electromagnetic or inertial.

The first CAS systems, dating back to mid-80's with the introduction of frameless stereotaxy, heavily relied on position sensing devices. At that time, mechanical digitizer represented a well-established technology to provide accurate position information. Mechanical digitizers consist of articulated arms, which determine the position of the tip by measuring changes in arm angle and/or length from an initial zero point.

Mechanical digitizers facilitated the first frameless stereotaxy systems by localizing either an operating microscope's focus or a surgical probe inside the patient's head, and, more recently, have been also used in ENT surgery (Freysinger et al., 1998).

Due to the cumbersome nature of mechanical digitizers of the time, interest in alternative tracking technology led to the introduction of ultrasonic transducers for localization (Reinhardt and Zweifel, 1990) (Barnett et al., 1993) (Bucholz and Smith, 1993). Sonic localization systems consist of receivers placed in a fixed geometry and a source of sound, beyond

the human audible frequency, emitting pulses. The distance between emitter and receivers is computed measuring the time taken for the sound to reach each receivers. The major drawback of this technology is that changes in environment temperature and humidity modify the speed of sound causing significant localization errors.

Given the issue with the speed of sound, an intuitive alternative is to change medium and use light. Optical tracking systems (OTSs) can be classified as follows (see Fig. 1.1):

- *Videometric tracking systems,* which identify marker patterns on video image sequences using one or more calibrated video cameras. Examples are the tracking system integrated in VISLAN, an integrated neurosurgical planning and guidance platform, and the Micron Tracker (Claron Technology Inc., Canada).
- *Infrared-based tracking systems,* consisting of two planar or three linear charge-coupled device (CCD) camera with an optical band-pass filter that eliminates all ambient light of wavelength other than IR. Depending on the type of marker to be tracked, these system can be further subdivided in:
    - *Active optical trackers.* Markers consist of sterilizable infrared light-emitting diodes (IREDs), which are sequentially fired and detected by each CCD unit. A central processing unit computes the 3D position of each marker using a triangulation process. A minimum of three non-collinear IREDs are necessary for determining six degrees-of-freedom (DOF) pose information. Since IREDs must be powered active systems are also wired system.
    - *Passive optical trackers.* Markers consist of retro-reflective spheres, illuminated by the camera in the near-IR spectrum. Geometrical arrangement of markers on the tracked body must be unique to allow for unambiguous assignment of object pose data. The main advantage is that no wires are needed between the tracked object and the tracking system.

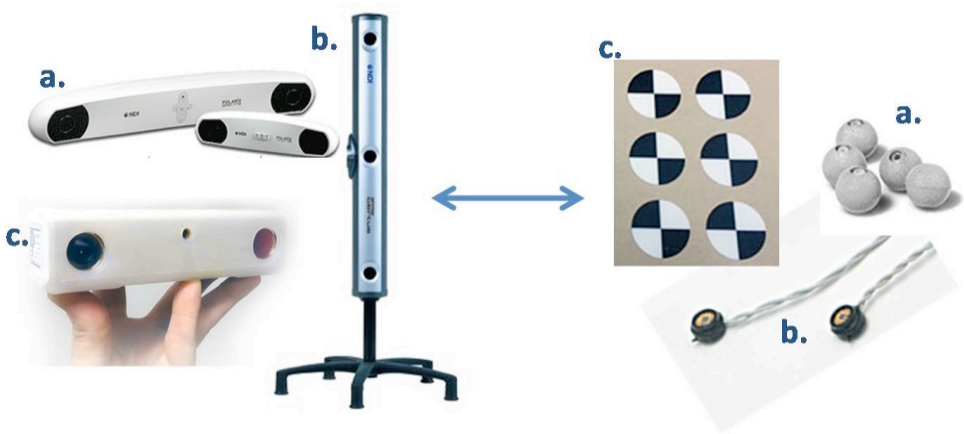

Fig. 1.1 – Examples of commercial OTS (left) with their respective markers (right). NDI[1] Polaris (a) is an example of passive optical tracker, whereas NDI Optotrak Certus (b) localizes infrared light-emitting diodes. The Micron Tracker (c) by Claron Technology[2] is an example of videometric tracking system, which recognizes predefined chessboard-like patterns.

OTSs are considered the de-facto standard tracking technology for clinical environments due to their high accuracy and reliability. The key limitation with the use of OTSs in a crowded OR is the line-of-sight requirement between the optical markers and the tracker camera, which led to the development of alternative tracking technology such as electromagnetic tracking systems (EMTS).

EMTS are a relatively new tracking technology in medical applications (see Fig. 1.2). These systems localize small electromagnetic field sensors (coils) in an electromagnetic field of known geometry. The EMTSs used in surgery can be divided in three main categories:

- *AC-driven tracking*. Probably the most common technology, these systems are driven by alternating current (AC). In the simplest configuration, the field generator consist of three coils arranged in a Cartesian coordinate system that emits three dipole field, with frequencies typically ranging from 8 to 14 kHz. Small sensing coils measure the induced voltage, which is proportional to the flux of the magnetic field (Kuipers, 1980). Commercially EMTS are available from Polhemus Inc. (VT, USA) and Northern Digital Inc. (Ontario, Canada).

[1] www.ndigital.com

[2] www.clarontech.com

- *DC-driven tracking.* These systems are driven by quasi-static direct current (DC) and are a concept by Ascension Technology Corporation (VT, USA). The magnetic induction within miniature active fluxgate sensors is measured after the establishment of a stationary magnetic field.
- *Passive or transponder system.* These systems localize permanent magnets or implanted transponders. Passive systems are relatively new and have been used in medicine to localize nasogastric feeding tubes (Bercik et al., 2005) or for tumor tracking during radiation therapy (Willoughby et al., 2006).

Despite the major advantage of not requiring line-of-sight, EMTSs provide less accuracy as compared to OTSs and suffer from magnetic field distortion due to ferromagnetic material or electrically powered devices within the measurement volume.

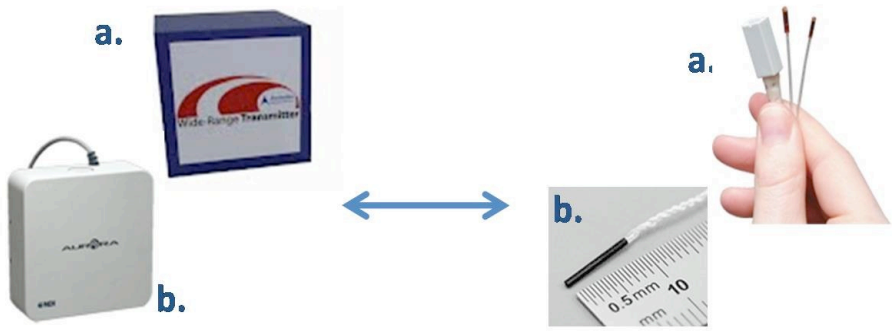

Fig. 1.2 – Examples of commercial EMTS transmitters (left) with their respective sensors (right). Ascension[3] trackSTAR (a) is an example of DC driven EMTS, whereas NDI Aurora (b) is an AC driven EMTS.

Another potential tracking solution is to combine three orthogonal accelerometers and three orthogonal gyroscopes, in a so-called Inertial Measurement Unit (IMU), to measure three-dimensional acceleration and angular velocity of the tracked object. Since acceleration and angular velocity are the second and the first derivative of position and orientation respectively, integration from a known starting point yields translation and rotation. Inevitably, small measurement errors, cause localization error to

[3] www.ascension-tech.com

increase over time. Despite this limitation, IMUs allow for the determination of position and orientation of an object at a high sample rate, raising the interest of researchers in biomechanical setup for joint motion (Zhou et al., 2006) and as auxiliary sensing device in hybrid motion tracking systems (Ren et al., 2011).

Force sensors are involved in several studies for biomechanical characterizations of tool–tissue interactions (Abolhassani et al., 2007).The main application of force sensors is to provide haptic feedback to tele-operated surgical robots (Rossi et al., 2005) and they rely on different technologies, such as strain gauges (De Lorenzo et al., 2010) (Berkelman et al., 2003), optical fibre (Puangmali et al., 2010) (Tan et al., 2011), capacitive-based, piezoelectric-based and vibration-based force-sensing (Puangmali et al., 2008).

Intra-operative imaging devices include magnetic resonance imaging (MRI), computed tomography (CT), fluoroscopy and ultrasonography (US), which are used to update the preoperative images and provide more information to the surgeons; this is of the utmost importance when dealing with soft tissues (e.g. brain) that undergo modification with respect to preoperative images during the intervention (Clatz et al., 2005) (Ohue et al., 2010). Additionally, recent developments in high-definition digital endoscopy offer an opportunity for vision-based navigation in image-guided interventions, such as laparoscopy, trans-nasal skull-base neurosurgery and natural orifice trans-luminal endoscopic surgery (NOTES) (Mirota et al., 2011).

1.4 Open issues

Despite technological advancements, the surgical practice is still constrained by the limitations of the human capabilities and approach variability. In some cases, this limitation is due to a lack of basic knowledge of the anatomical structures to be operated on, as in the case of certain brain interventions. In many cases though, the limitations are due to surgeon inability to operate in the confined space of the human body, to perform the

correct diagnosis of the patient pathology, or to quickly react to sudden situation changes.

Given the proved advantages of providing the surgeon with additional pre- and intra-operative information, the adoption of sensing technology in modern CAS systems is not free from risks and drawbacks though. Issues arise due to the peculiarity of the operating theater, which is a complex, delicate and crowded environment.

Furthermore, the limitations of currently available tracking technologies affect their usability in modern over-crowded ORs and in the fast control loop of a surgical robot.

Tracking systems for surgical applications should be evaluated in terms of:

- *Accuracy.* This, of course, depends on the application; typical values for most applications are around 1 mm for translation and few degrees for rotations, up to the most demanding neurosurgical procedure where localization error less than 1 mm is required.
- *Robustness.* This concept is strictly related to the safety of the procedure, and entails, for instance, a continuous data stream.
- *Update rate.* This has only recently gained attention with the introduction of robotic systems. Current tracking technology, typically have update rate of few tens of Hz, which ensure good results for standard navigations systems. In case of a control loop of a surgical robot in contact with the patient, the feedback information must be provided at several hundreds of Hz.

Based on these parameters, OTSs present high accuracy but their robustness is limited by the line-of-sight requirement. On the other hand, EMTSs accuracy is affected by electromagnetic disturbances but they are able to measure position and orientation of tools inside the body without any line-of-sight requirement. Both OTSs and EMTSs, though, provide data at a relatively low update rate for robotic applications, whereas IMUs are able of acquisition frequency around 1 kHz, but the integration of acceleration and angular velocity data leads to accumulating errors. Main limitations of the aforementioned sensing technologies can be overcome by their combined

use. To this extent information sources must be first correctly synchronized and then fuse together, usually with a probabilistic approach.

The management of multiple sensors with different frame rates and spatial scales entails a data fusion process in both time and space. Using a software-based application for time-stamping external information induces a temporal imprecision, which can be due to the offset of the PC clock with respect to a reference time and to the drift of the internal clock (frequency error) (Kais et al., 2006). Attention should be paid to spatial consistency as well, since each sensor has its own reference system and spatial scale; spatial transformations between reference systems can be estimated with calibration procedures (De Momi et al., 2008), (Schwald et al., 2004).

The goal of this thesis was to investigate methodologies for the management and integration of multimodal sensors in surgical applications and to develop a software framework for sensors data acquisition and fusion.

The thesis is organized in two main chapters. The first part of the work concerns the software framework for sensors management and it was carried out at NearLab, Politecnico di Milano, Italy, within the European research project ROBOt and sensors integration for Computer Assisted Surgery and Therapy (ROBOCAST) FP7-ICT-2007-215190. The second part is mainly focused on the optical line-of-sight occlusion problem. A preliminary study on the Unscented Kalman Filter technique and model-based robust optical tracking was carried out during my stay at Kitware Inc., Carrboro, NC, USA. The proper sensor fusion algorithm was developed at NearLab while still collaborating with Dr. Enquobahrie at Kitware.

Chapter 2

Data acquisition framework: the "Sensor Manager"

This chapter highlights the main issues in the management of the plethora of available sensing technologies for CAS systems. A centralized architecture, based on the open-source "Image-Guided Surgery Toolkit" (IGSTK), is presented and validated in a real architecture for computer and robot assisted surgery made available by the ROBOCAST project (FP7 ICT-2007-215190)

2.1. Background

As already pointed out in Chapter 1, Surgical navigation involves a) a registration process between physical space and pre-operative images space and b) intra-operative localization of the surgical tool in order to show position and orientation of the instrument with respect to anatomical structures. To this extent, different types of sensors (see §1.3) are widely used and provide surgeons with multimodal information.

The need for libraries for the simultaneous management and integration of sensors information has recently arisen. In the surgical field, this has led to the design of a software framework for tracking system management and surgical navigation application prototyping, known as the Image-Guided Surgery Toolkit (IGSTK)[4] (Enquobahrie et al., 2007), (Ibanez et al., 2008), (Yaniv et al., 2010), an open-source project continuously expanding to also include other types of sensors (e.g. video and ultrasound images).

Furthermore, modern CAS systems often rely on multiple sensors from the aforementioned categories in order to ensure redundancy in case of failure and to provide different information to increase surgeons' perception. For instance, Tobergte et al. (2009) proposed a data fusion algorithm, using an

[4] http://www.igstk.org

optical localization system and an IMU, to overcome line-of-sight occlusion and achieve a higher update rate in order to perform patient motion compensation with a robotic system. The combined use of an ultrasound imaging device and a localization system (typically an optical one) to achieve a 3D volume reconstruction (Freehand 3D Ultrasound) (Unsgård et al., 2011), has been proposed for brain shift estimation in neurosurgery.

The management of multiple sensors information with different data generation rates and space scale entails a data fusion process both in time and space, in order to extract consistent information. Timing aspects are crucial in a multiple sensor scenario since each data needs to be correctly synchronized to the other. Using a software-based application for time-stamping external information induces a temporal imprecision, which can be due to the offset of the PC clock with respect to a reference time and to the drift of the internal clock (frequency error) (Kais et al., 2006). Spatial consistency is also required when dealing with different sensors information; spatial transformations between reference systems are obtained with calibration procedures (De Momi et al., 2008), (Schwald et al., 2004).

Most CAS systems were traditionally controlled by a single computer and program. Recently, Peters et al. (2005) proposed a modular, distributed approach, which was also adopted in the EU-funded project ROBOCAST (FP7 ICT-2007-215190) (De Momi and Ferrigno, 2010); such architectures make it easy to add features, replace devices, or reuse components of a CAS system. Synchronization and spatial consistency issues, which occur when different clocks and several reference systems are involved, were addressed. Communication between components in distributed systems is in charge of a middleware layer, which enables transport of network independent communication without time-consuming adaptations and re-development of domain applications (Reintsema et al., 2011). Following the classification proposed by Emmerich (2000), surgical distributed architectures usually rely on object-oriented middleware, such as the Common Object Request Broker Architecture (CORBA) (Peters et al., 2005), (Tanaka et al., 2004), (Mönnich et al., 2009). As an alternative, transaction-oriented and message-oriented middleware may be used, though they are mainly used for distributed

databases. The publish/subscribe pattern (also known as pub/sub) is part of a message-oriented middleware. In a pub/sub architecture, senders (publishers) and receivers (subscribers) are loosely coupled and have almost no knowledge about each other: for certain applications this can be an advantage, allowing a dynamic network topology. However, this raises safety issues since possible crash of a publisher or a subscriber application will not be notified to the other (Eugster et al., 2003).

In this study, we propose an IGSTK-based, multi-sensor management system for a distributed CAS architecture based on object-oriented middleware that addresses information consistency in both space and time. The aim of this work is to integrate the IGSTK library in a modular architecture for CAS, to verify the satisfaction of clinical requirements and to test the applicability of such framework in a real CAS setup.

The choice of an open-source framework like IGSTK ensures a very well maintained source code, the support of a worldwide community of users and developers, and the possibility of customization and extension of the toolkit features. Compared to utilizing commercial products, the use of open-source platforms allows reducing costs.

The system was validated within a CAS system for robotic neurosurgery in order to verify the suitability of the proposed central sensor management system for neurosurgery applications and to measure the latency in a client/server architecture.

2.2 The CAS system

The proposed sensor management architecture was developed and tested within the distributed CAS system of the ROBOCAST project. ROBOCAST combines navigated and robotic approaches (see Fig. 2.1) to address minimally invasive neurosurgery procedures (e.g. biopsy) through a small aperture in the skull (keyhole neurosurgery). In ROBOCAST, three robots connected in a kinematic chain (13 degrees of freedom) are used to optimize the positioning accuracy (Comparetti et al., 2011).

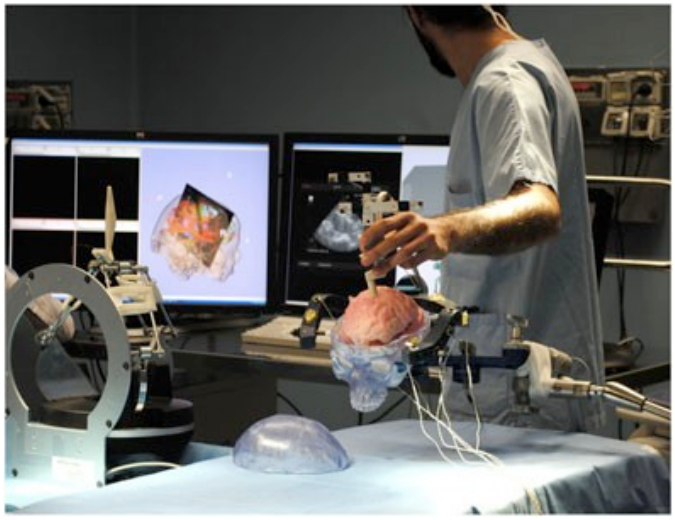

Fig. 2.1 - The ROBOCAST demonstrator used in phantom trials at Ospedale Maggiore, Verona – Italy. The operator is maneuvering an ultrasound probe, while looking at the intra-operative visualization monitors. The US image is superimposed on the pre-operative brain models.

System accuracy and safety are extended by means of different sensors: an active marker OTS, *NDI Optotrak Certus* (NDI Inc., Ontario, Canada) which surveys the overall robotic chain; an EMTS, *NDI Aurora* (NDI Inc., Ontario, Canada); and an ultrasound imaging device, *Prosound Alpha 7* (Aloka Co., Ltd., Japan).

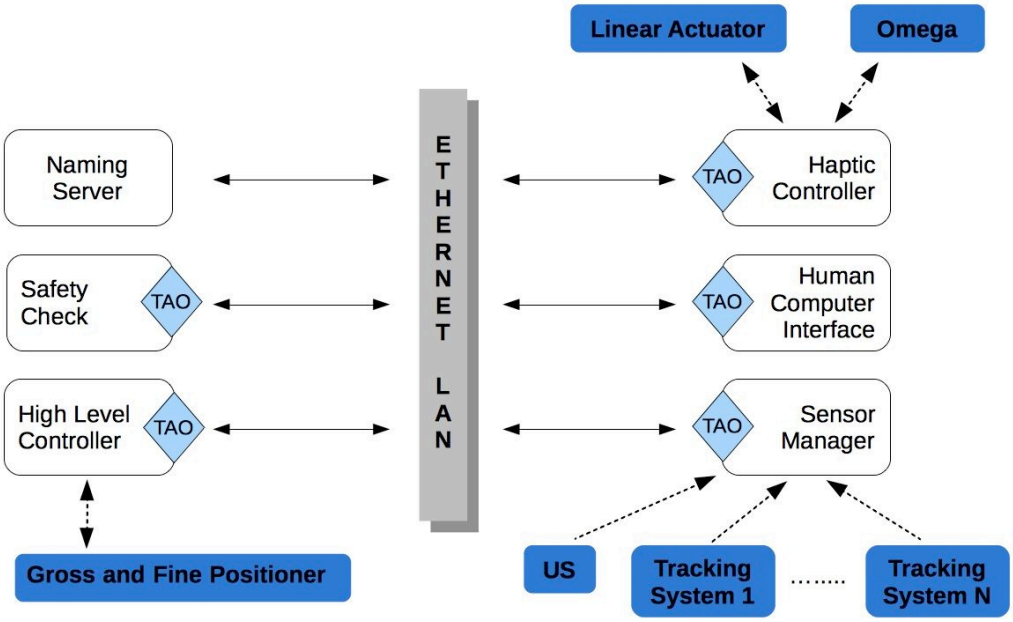

Fig. 2.2 - The ROBOCAST distributed architecture. Hardware devices, grey boxes, are connected to their respective controllers. A middleware layer (TAO - The ACE ORB), over a Gigabit Ethernet LAN, manages the communication of data and services between each software module of the system. The Sensor Manager (SM) is in charge of data acquisition from ultrasound imaging device and localization systems.

The main components of the ROBOCAST distributed architecture, shown in

Fig. 2.2, are:

- *Naming Server* (NS), similar to a Domain Name System (DNS) of the ROBOCAST network, which translates domain names into the respective numerical identifiers.
- *Safety Check* (SC), a process that periodically checks for consistency of the calibration and registration transformations and for possible occlusion of the OTS line-of-sight.
- *High Level Controller* (HLC), in charge of robots control.
- *Haptic Controller* (HC), which controls a *Linear Actuator* motion according to a haptic device input and manages force information.
- *Human Computer Interface* (HCI), which provides a surgeon interface for intra-operative navigation and workflow execution.
- *Sensor Manager* (SM), an IGSTK-based application that gathers tracking data and US images and provides them to the other components upon request.

The middleware of ROBOCAST is *The ACE ORB* (TAO)[5], a freely available, open-source, and standards-compliant, real-time C++ implementation of CORBA based upon the Adaptive Communication Environment (ACE)[6].

2.3 The Sensor Manager

The SM is a software component within the distributed architecture of the ROBOCAST system (Vaccarella et al., 2011 CARS). It is implemented as a C++ service application without a user interface running on a dedicated machine. The main purpose of the SM is to gather data from localization systems (optical and electromagnetic) and US imaging devices, and forward such information upon request to the other components of the system (clients). As is each component of the ROBOCAST framework, the SM is part of a client/server architecture based on the middleware TAO CORBA.

[5] http://www.theaceorb.org

[6] http://www.dre.vanderbilt.edu/ACE

The SM encompasses two main parts; 1) interfacing the hardware based on the open source libraries IGSTK and OpenCV[7] and 2) acting as server to provide data and services to other modules in a CORBA-based network architecture. Also, an processing layer is provided to manage reference frame transformations. The registration/calibration (e.g. between optical and electromagnetic reference system) was performed using algorithms developed by De Momi et al. (2008), whereas patient registration to preoperative image space was accomplished using the method by Horn (1987). IGSTK is mainly used for spatial relationship hierarchy definition among reference frames and for tracking data acquisition. IGSTK provides software components to implement a spatial object hierarchy, which facilitates spatial transformation computation between couples of reference frames. This allows clients to ask for the transformation matrix of a reference system associated with an object in the ROBOCAST scenario, with respect to other reference systems.

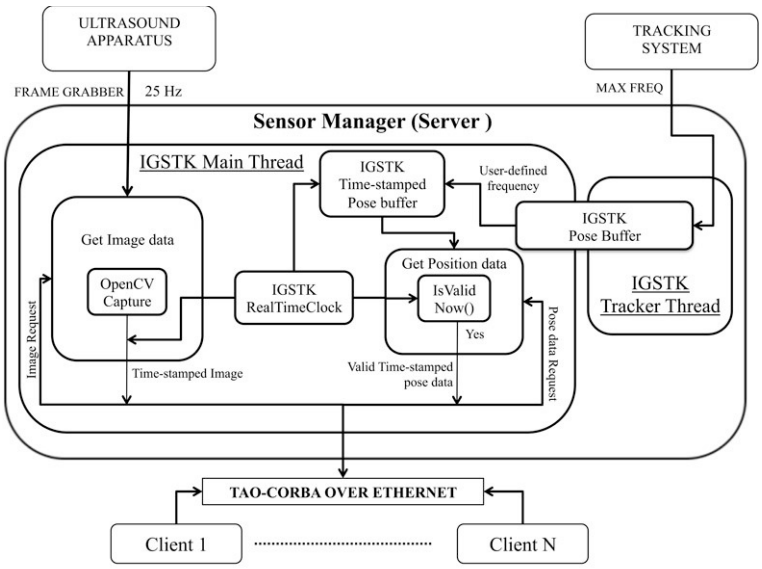

Fig. 2.3 - The SM data acquisition architecture. A separate Tracker Thread is spawned for each tracking system in order to continuously store new data in a buffer. The buffer is shared with the application Main Thread where data are time-stamped by the IGSTK RealTimeClock and copied in another buffer. Through the IsValidNow() block, pose data are delivered to the client only if less than K ms elapsed since data was acquired (K=user-defined threshold). Upon request pose data delivered to the client after a temporal validity check with a user defined threshold. US image requests are managed in the main tracking thread with the OpenCV capture module and time-stamped by the IGSTK RealTimeClock.

[7] http://opencv.willowgarage.com

The SM can transparently manage all the IGSTK supported tracking devices through an XML configuration file, allowing flexibility in hardware arrangement.

According to the IGSTK architecture, as shown in Fig. 2.3, tracking data is continuously acquired in a separate thread (*Tracker Thread*, one for each tracking systems) and stored in a buffer. The main thread updates spatial objects transformation by reading the stored tracking data from the buffer at a user-defined frequency (20 Hz), and marks each data with a timestamp provided by the IGSTK *RealTimeClock*. Pose data is checked for temporal validity prior to being provided to clients; the IGSTK *IsValidNow()* function compares the current time (read from the *RealTimeClock*) and the timestamp associated with the pose data, and forwards the information to the client only if it is less than K ms elapsed since data acquisition (K is a user-defined threshold).

Open-CV allows the acquisition of images from US imaging devices, which are connected to the SM laptop via an USB frame grabber (EZ-Grabber, PAL: 720 x 576 @ 25 fps). US images are time-stamped using the same clock used for tracking data (IGSTK *RealTimeClock*).

2.4 The experimental protocol

The IGSTK-based application was validated in a modular and distributed CAS system. Experiment #1 was aimed at comparing time intervals measured with different clocks in the ROBOCAST distributed architecture. Experiment #2 computed the SM latency.

2.4.1 Experiment #1

The optical localization system (Certus, NDI Inc., Ontario, Canada) was connected to the SM (SERVER), and two client machines (CLIENT1 and CLIENT2) were set-up to request localization data. The three computers specifications are listed in Table 2.1. Each machine was connected to a Gigabit Ethernet LAN in the ROBOCAST, CORBA-based client/server architecture.

The reference time for the experiment was provided by the SM based on the timestamp of localization data. CLIENT1 and CLIENT2 internal clocks (based on MS Windows API) were compared with the reference time in order to explore inter-machine variability. Since Windows NT operating systems' internal timer resolution is 10-15 ms (47), a higher resolution is achieved by accessing the High Precision Event Timer (HPET) incorporated in PC through the Windows API; for each machine in our setup, the frequency of the HPET proved to be nominally 3.57 MHz with a microsecond resolution.

Table 2.1 - Specifications of computers involved in the tests

	CPU	RAM	OS
SM	Intel T7600 @2.33 Ghz	2 GB	MS Windows XP Professional, SP3
CLIENT1	Intel Q9550 @2.83 GHz	3 GB	MS Windows XP Professional, SP3
CLIENT2	Intel E6600 @2.4 GHz	2 GB	MS Windows XP Professional, SP3

SM and CLIENT clocks were started and stopped together in order to measure six different time intervals ΔT_i (15, 30, 45, 60, 75 and 90 minutes).

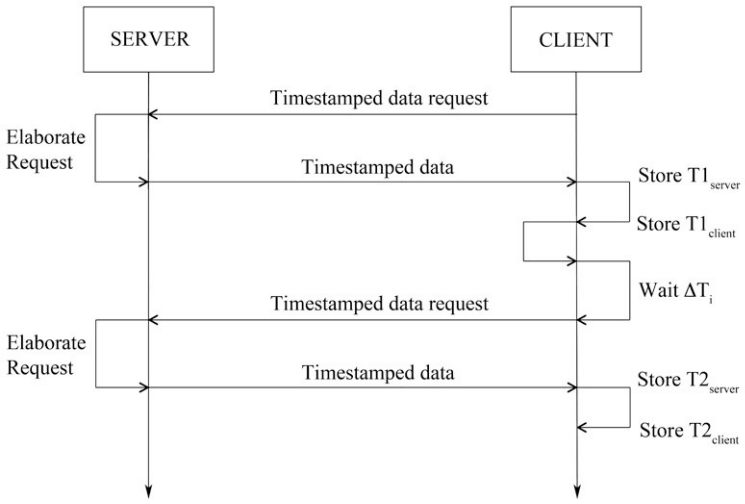

Fig. 2.4 - Experimental protocol to compare ΔTi measured with different PCs: the CLIENT receives time-stamped data and compares SERVER timestamp with its internal HPET time.

The test protocol is summarized in Fig. 2.4.

When the client requests tracking data, the SM, based on the IGSTK

framework, provides data and timestamp information; the client receives the data and the timestamp ($T1_{server}$) and also stores its current time according to the internal HPET ($T1_{client}$). After the time interval ΔT_i, the same pattern is repeated and $T2_{server}$ and $T2_{client}$ are stored in order to compute ΔT_{client} ($T2_{client}$ - $T1_{client}$) and ΔT_{server} ($T2_{server}$ - $T1_{server}$). The difference (ΔT_{client} - ΔT_{server}) between each couple of time measurement is stored.

The experiment was repeated ten times for each ΔT_i and for both CLIENT1 and CLIENT2.

2.4.2 Experiment #2

In the following experiment, the latency of the SM responses is evaluated in case of tracking data and US images requests by clients.

The experimental setup encompasses:

- Two PCs, SM, and CLIENT1 (see Table 2.1 for details) connected to the CORBA-based ROBOCAST network.
- An active markers OTS, NDI Optotrak Certus.
- A passive markers OTS, NDI Polaris Vicra (not used in ROBOCAST).
- An EMTS, NDI Aurora.
- An ultrasound imaging device, Aloka Prosound Alpha 7.

The protocol was the following: the CLIENT1 clock (based on its internal HPET) measures the time ($\Delta T_{latency}$) elapsed from the instant a data request is issued to the SERVER to the instant data are received by the client. The experiment was repeated 6000 times for each tracking system and for the US imaging device.

2.5 Results

2.5.1 Experiment #1

Fig. 2.5 shows the differences ΔT_{client} - ΔT_{server} for CLIENT1 and CLIENT2. Mean and standard error of ten repetitions is reported for each ΔT_i. The absolute value of the error linearly increases with the time interval ΔT_i. Linear regression was also calculated with reference to the IGSTK

RealTimeClock running on the SM (SERVER); the CLIENT1 internal clock resulted being slower (about 1 ms/min), while the internal clock on CLIENT2 proved to be faster (about 2 ms/min).

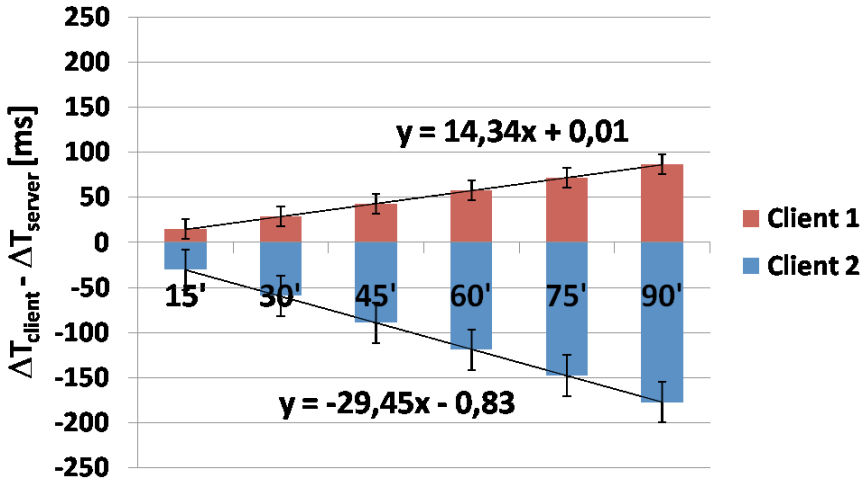

Fig. 2.5 - Time measurement comparison using the SM and two different clients: each column in the graph represents the mean with the associated standard error of ten repetitions. Linear regression equations are reported.

2.5.2 Experiment #2

The latency of the SM in providing data to clients is shown in Fig. 2.6. Since the data distribution resulted in being non-Gaussian (Lilliefors test, $p < 10^{-3}$), median values (with interquartile ranges) were computed. Latency for tracking data resulted in being about 2 ms and does not depend on the tracking system used (Kruskal-Wallis test, $p > 0.5$). US images showed a latency of about 40 ms.

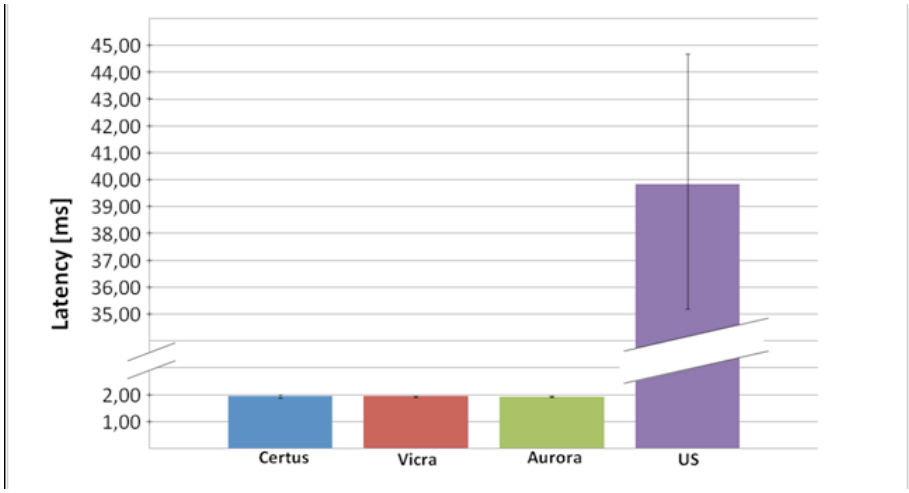

Fig. 2.6 - SM response latency for tracking data and US images requests

2.6 Use case: 3D Ultrasound temporal calibration

We choose three-dimensional (3D) Ultrasound (US) as paradigmatic example application of the proposed SM architecture and proved its feasibility in the ROBOCAST final demonstrator.

3D US imaging is a non-invasive medical diagnostic method that is recently gaining importance as intra-operative imaging in surgical procedures, where organs or soft tissues morphology varies with respect to the pre-operative situation. In neurosurgery, for example, US images of the brain are registered with preoperative Magnetic Resonance imaging (MRI) to determine the brain shift occurring during the operation (Gronningsaeter et al., 2000), (Lindseth et al., 2003), (Unsgård et al., 2011). 3D US imaging is used also in radiotherapy (Wong et al., 2011) and abdominal surgery (Johnston et al., 2008), (Mozer et al., 2005). 3D ultrasound imaging can be build from 2D images by tracking the position of a probe in space, by a mechanical, optical or electromagnetic localization system and associating each US scan with the respective probe pose in 3D space. To ensure accuracy of the reconstruction, temporal alignment of tracking data and US images is a demanding requirement (Jacobs and Livingston, 1997); this is achieved estimating the overall latency between images and tracking data through a temporal calibration procedure.

The experimental setup, shown in Fig. 2.7, is composed by an active marker OTS, NDI Optotrak Certus (Northern Digital Inc., Canada), an ultrasound imaging device, Prosound Alpha 7 (ALOKA Co., Ltd., Japan), and a six Degrees of Freedom (DoF) serial robot, PathFinder (Prosurgics, UK).

In order to estimate the temporal offset between the DRF tracking data and the US image, the probe immersed in the water tank was moved along the vertical direction using the PathFinder serial robot, which was programmed to achieve 3 repetitions of vertical motion (lasting 0.83 s at 30 mm/s constant velocity); the experiment was repeated ten times.

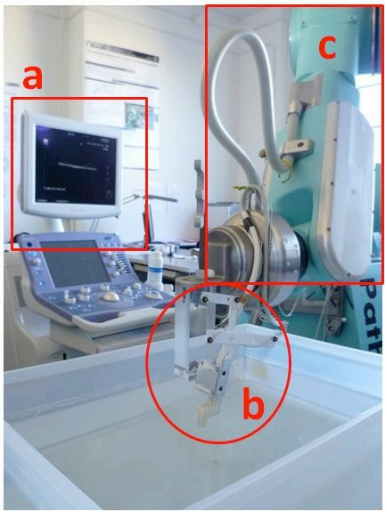

Fig. 2.7 - 3D US temporal calibration setup. An US imaging device (a) is used to acquire images from an optically tracked (OTS not in the picture) US probe (b) while it is vertically moved in a water tank by a serial robot (c).

The bottom of the tank is represented on the US image as a line; the distance of the line from the top of the image is computed for each frame so that a mono-dimensional signal is obtained. Position data of the probe DRF was acquired at the same time and normalized with respect to the amplitude of the movement performed. The two signals were aligned using the timestamps provided by the SM application and the time lag was estimated by computing the maximum of the cross-correlation function of the two time series.

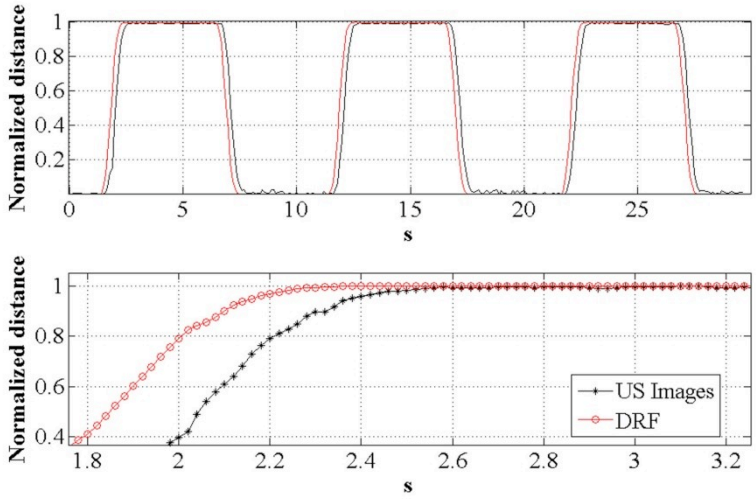

Fig. 2.8 – Normalized distance signal computed from US images (black) and OTS (red). As shown in the enlargement below and confirmed by cross correlation analysis, the relative lag is about 0.2 s.

As shown in Fig. 2.8, the time lag between the DRF data and the US image resulted in a median value of 230 ms (223 ms and 240 ms the inter-quartile range). Results show that such architecture does not allow, at this stage, real time volume reconstruction, since post-processing of data is required for proper time alignment, on the basis of the presented temporal calibration. Nevertheless a slow exploration (few mm per second) is indeed possible and useful whenever soft tissue interaction is involved, for instance during neurosurgical procedures to update the pre-operative plan once brain-shift has occurred.

2.7 Discussion

All innovative systems for surgery assistance require sensor information integration in order to effectively carry out the procedure with an increased accuracy and safety, both for patients and operators.

In this Chapter, we presented a centralized software application for the management of multiple sensors within an integrated robotic and navigated platform for neurosurgery based on IGSTK.

Within the ROBOCAST project, the SM was designed to acquire, timestamp, process, and broadcast data from localization systems (optical and electromagnetic) and from a US imaging device to other software modules distributed over a Local Area Network. Moreover, a modular and general-purpose approach was adopted, rather than one tailored to the hardware, allowing interchangeability of sensors and seamless integration of more than two sensors. The main challenge of such an application is to provide consistent data from different sensors both in terms of spatial relationship and synchronization, keeping the latency within a desired limit depending on the clinical application, and without affecting the actual hardware frame rate.

The IGSTK open-source library proved to be suitable for meeting the previous specifications. In particular, IGSTK encourages the development of hardware-independent applications and provides support for a wide range of localization systems; additionally, being an open-source project makes it possible to extend features as was done for the NDI Optotrak Certus, which was not initially supported (Vaccarella et al., 2010 CARS). IGSTK also

provides software tools to manage spatial relationship hierarchies, which facilitate the development of computer integrated surgery applications. This is relevant in a multi-sensor robotic system for surgical applications, such as ROBOCAST, where multiple reference frames are involved (preoperative images, optical, electromagnetic, US images, actuators' reference frames). Once the calibrations between different spaces are provided, the SM automatically handles relative spatial transformations. The IGSTK *RealTimeClock* module is used as a common reference to timestamp data acquired from all sensors (both tracking systems and US imaging device).

Synchronization in distributed architectures usually entails timestamp exchanges and transformations between different computers. Bezet and Cherfaoui (2005) achieved synchronization by exploiting a synchronous bus network (the FireWire, IEEE 1394); the bus clock is used to estimate the drift of all computer clocks in order to exchange data timestamps with high precision and to compute time equivalences between the different clocks for post-processing time-stamping synchronization.

When dealing with Ethernet communication, as in the case of the ROBOCAST architecture, the communication bus does not carry synchronization information. In Experiment #1, we proved that in such conditions, the presence of different clocks is not acceptable as it leads to time drift due to clock offset and an unpredictable combination of quartz inaccuracies that depend on the operating temperature and manufacturing process; the frequency tolerance for the single quartz is typically in the range of $\pm(10 - 100)$ ppm. The present work proposes the use of a unique time-stamping module for all sensors to avoid inaccuracy due to the offset between different clocks. It would also ensure a frequency drift within the tolerance of a single quartz, meaning an error of $9 \div 90$ ms every 15 minutes; such an error can be considered tolerable depending on the specific application. For example, in the ROBOCAST scenario where an optically-tracked linear probe is advanced in the brain at a maximum velocity of 2 mm/s, the maximum localization error of the surgical tool due to clock drift is therefore 180 μm in case of a 15 minutes acquisition; this is negligible compared to neurosurgery requirements and robot targeting accuracy

(Comparetti et al., 2011).

The proposed SM, as part of a modular system, is also ready to be used in other possible architectures, thanks to the middleware abstraction layer. For example a SM module can be instantiated for each sensor node (in order not to limit acquisition bandwidth) and a central SM would take care of processing data synchronized via Precision Time Protocol (PTP) (Correll et al., 2005). We actually tested the worst-case scenario, where all the sensors were connected to the same acquisition workstation, which was also in charge of sensor data processing and integration. Furthermore, since we proved the feasibility of the proposed approach within the ROBOCAST scenario, which is a paradigmatic example of an advanced CAS system, it is expected that also other applications (e.g. endoscopy or MRI-guided surgery) would be satisfied by our architecture.

The client/server architecture based on TAO-Corba was preferred to a pub/sub approach mainly for safety reasons. The pub/sub approach is reported to be unsafe since application crash cannot be detected due to the decoupling of publisher and subscriber, which is not acceptable for life critical application such as CAS. This issue could be handled at application level (e.g. each application emits a periodic heartbeat) but this would increase complexity and bandwidth consumption. Whether client/server or publish/subscribe makes the most efficient use of bandwidth is a nuanced issue. On the one hand, publishers continuously stream data over the network, regardless clients ask that information or not. This can lead to unwanted bandwidth consumption, whereas in a client/server architecture the bandwidth is occupied only upon client request. On the other hand, a client/server approach requires twice as much network traffic to get a result (request and reply). However, in CAS applications, the need and the update rate of sensor data can vary depending on the step of the surgical workflow (e.g. registration/calibration, navigation etc.).

Experiment #2 was designed in order to assess the overall latency for a client to receive requested data. The processing introduced by the SM must be transparent to the client, not limiting the actual hardware frequency. Results of Experiment #2 showed a response latency of about 2 ms for each

tested tracking system. With this latency, the client can issue up to 500 requests per second -- much faster than data generation rate of the majority of commercial tracking systems (NDI Optotrak Certus is the only tracking system that can reach frame rate higher than 500 Hz if less than seven markers are connected). It is relevant that this result does not depend on the tracking system; any possible, subsequent elaboration of tracking data can be designed regardless of the hardware in use. Other types of sensors could be integrated as well (e.g. force sensors, IMUs, etc.).

Latency for US images proved to be around 40 ms, which is limited by the frame grabber acquisition rate (25 fps); whenever a higher frame rate is required for high-speed movement tracking or tissue elastography (Park et al., 2006), a tailored high frame rate acquisition hardware must be adopted (Dai et al., 2010). The same latency is expected for any other kind of images with the same pixel number.

In ROBOCAST, a synchronous communication model (Peters et al., 2005) was adopted, which means that the application execution on the client is blocked until a response from the server is received. Thus, the latency observed in Experiment #2 includes request transmission time, request elaboration on the SM, and response transmission time.

We also presented a possible application to 3D US where the SM module assures data synchronization in time-stamping US probe position data and US images (only 17 ms of inter-quartile range shows the delay is approximately constant).

The object-oriented middleware, TAO, provided an abstraction layer, which enables developers to skip low-level implementation of the communication protocol. It proved to be agile and did not introduce significant delay in the communication. Furthermore, with such a distributed architecture many clients can simultaneously access the sensors, which is an important starting point towards the development of increasingly sophisticated CAS applications.

Chapter 3

Sensor fusion

This chapter will introduce the concept of multi-sensor data fusion reviewing methods and algorithms commonly adopted to this extent, focusing in particular on the Unscented Kalman Filter (UKF). An application of an UKF in the surgical scenario is presented to fuse together data from an OTS and an EMTS.

3.1. Multi-sensor data fusion

Among the variety of sensors used in the operative room for Image-Guided Surgery (IGS), OTS are the most widespread due to their ease of use and cost effectiveness. However, as showed in §1.3, OTS' suffer from the major drawback of line-of-sight requirements. Electromagnetic localization systems are also commonly used but in limited types of application due to their small working volume and relatively low accuracy.

The most common method to tackle the robust pose estimation problem is a state space approach based on different implementations of the Kalman filter. Simpson (Simpson et al., 2007), proposed an Unscented Kalman Filter (UKF) to estimate the pose of a surgical instrument based on optical active markers measurements. In (Halvorsen et al., 2005), an Extended Kalman Filter (EKF) based on noisy marker measurements was proposed to estimate rigid body pose with application to human motion analysis.

A different approach is multiple sensor fusion, which is more and more often adopted in surgical navigation and robotics applications to overcome limitations of current sensor technology since different types of sensors can complement each other and yield a more comprehensive description of the observed environment.

Chapter 3. Sensor fusion

Although one might consider sensors integration and sensors fusion as synonyms, a distinction needs to be done. Sensors integration refers to the synergistic use of multiple sensors to assist in the accomplishment of a task, whereas sensors fusion entails an actual combination of different information into one representational format (Luo et al., 2002). Sensors fusion may occur at any stage in the integration process, which may also not involve a proper fusion (e.g. information from one sensor may be used to guide the operation of others without an actual combination of the information).

The most commonly used algorithms to implement sensor fusion are based on 1) Kalman filters, 2) Bayesian networks and 3) Dempster-Shafer theory.

1) Kalman Filter (Sun and Deng, 2004) and its extensions to non-linear systems such as Extended Kalman Filter and Unscented Kalman Filter (Van der Merwe et al., 2004), are considered a natural way of implementing fusion between different sensors measurements. The Kalman filter is a linear dynamical system that attempts to mimic the behavior of an observed process (Rao, 1999). At each time instant, an optimal estimate of the current state of the observed process is computed. The estimate is used in conjunction with a model of the observed process to predict the next expected measurement. Given the next measurement, the filter computes the difference (or sensory residual error) between its prediction and the actual measurement, and uses this residual to correct its estimate of the state. The new corrected estimate is then used to predict the next state and to complete one full iteration of the filter. In case of non-linear models, modified versions of the Kalman Filter can be used (e.g. Extended Kalman Filter, Unscented Kalman Filter etc.).

As an example, an Extended Kalman Filter (EKF) has been used in virtual reality to combine the stable but low-frequency information of vision sensors with the high frequency motion tracking of inertial rate-gyroscope sensors to provide robust and accurate 6DoF pose tracking (You and Neumann, 2001).

An EKF data fusion using an optical localization system and an IMU has been proposed in (Tobergte, 2009) to overcome line-of-sight occlusion and

achieve a higher update rate in order to perform patient motion compensation in a robotic surgery framework.

EKF has been used also for a multiple-sensor fusion algorithm for a wireless hybrid tracking system that integrates electromagnetic sensing coils and IMUs: Ren et al. (2012) showed that integration drift of IMU can be successfully compensated by the measurements from the EMTS.

Other applications include robotic manipulator control (Jassemi-Zargani and Necsulescu, 2002) and mobile robot localization (Jetto et al., 1999).

2) Bayesian networks belong to the family of probabilistic graphical models used to represent a set of random variables and their conditional dependencies to express knowledge about an uncertain domain (Jensen, 1996). (Zhang et al., 2010) proposed a Bayesian network based multiple sensor fusion for a health monitoring system where a hierarchical approach was adopted for classifying features extracted from different sensors data. The limit of the previous approach is that every probability distribution in the system is assumed to be Gaussian or a mixture of Gaussian whereas a non-parametric representation would better approximate true distribution.

3) The Dempster-Shafer decision theory is considered a generalized Bayesian theory, which is the canonical method for statistical inference problem. It allows combining evidence from different sources and arriving at a degree of belief that takes into account all the available evidence. It has been also used for context-aware intelligent sensor fusion, like in (Wu et al., 2002) where an application to tracking the focus of attention of people in a conference meeting is showed: experiments showed that the capability to track people's attention with the fusion framework is significantly higher than single sensor's performance.

Aside from the previous algorithms, there exist several architectures for sensor fusion whose performances heavily depend on the application (Elmenreich, 2007).

Elmenreich (2007) distinguished between:

- Abstract models, which offer guidelines but not concrete implementation criteria;

- Generic architectures, which provide generic design without tailoring the implementation to a specific operating system, hardware or communication channel/protocols;
- Rigid architectures, which specify implementation aspects thus being less flexible.

An example of rigid architecture is the time-triggered sensor fusion model, which proposes a strictly synchronous design, where each task and communication activity is planned a priori in a static schedule (Kopetz and Bauer, 2003). The time-triggered approach works well with typical sensor fusion algorithms, such as Kalman filtering which requires periodic sets of measurements. An example is shown in (Elmenreich and Pitzek, 2001) where multiple distance sensors and a vision system allowed a mobile robot to reliably detect obstacles in the environment.

A common example of generic architecture is the JDL model, proposed by the Joint Directors of Laboratories under the guidance of the U.S. Department of Defense. The JDL architecture comprises five levels of data processing and a database, which are all interconnected by a bus, starting from Level 0 (Source Preprocessing) to Level 4 (Process Refinement) (Varshney, 1997). More recently (Blasch and Plano, 2002) added Level 5 (User Refinement) to better model "human in the loop" situations (see Fig. 3.1).

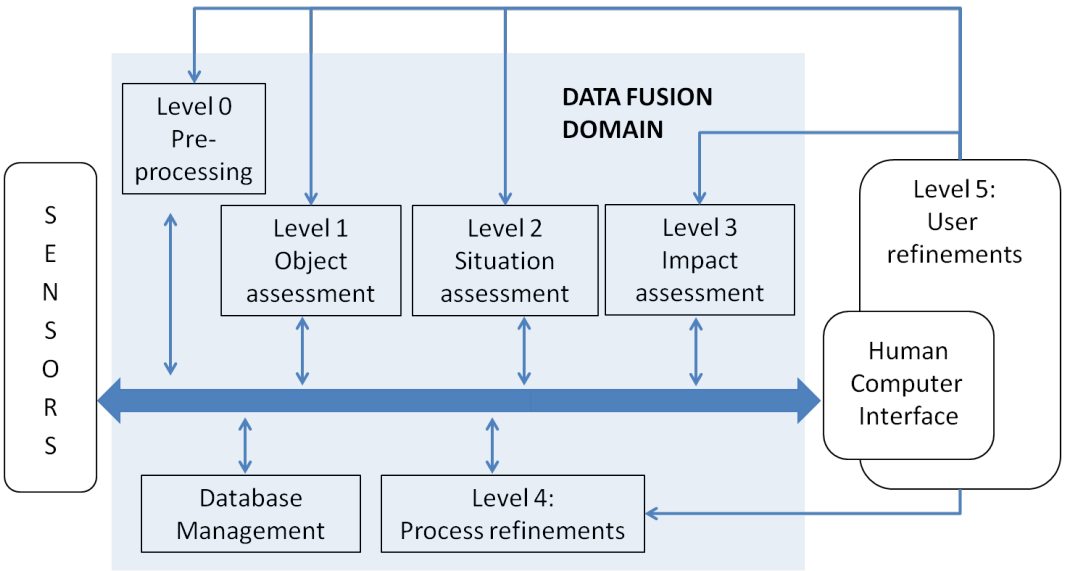

Fig. 3.1 - Blasch (2002) added Level 5 "User refinement" to the standard JDL data fusion model. Level 5 acts at every single stage of the data fusion process, modeling human in the loop situations.

More recently research efforts have been directed to the so-called cognitive sensor fusion, which is a biologically inspired approach to integrate multiple sensor data (Schmidt, 2010). One of the main goals of this approach is to provide artificial systems with situation or context awareness and high level reasoning capabilities, but this is outside the scope of this thesis.

3.2 The Unscented Kalman Filter

In control theory, a dynamical system is described by a set of two equations according to the state space representation (also known as "time domain approach"):

$$\begin{cases} x_k = f\left(x_{k-1}, u_k, w_k\right) \\ z_k = h\left(x_k, v_k\right) \end{cases} \tag{3.1}$$

where, **f()** is the state transition function, which predicts the current state $\mathbf{x_k}$ based on the previous state, $\mathbf{x_{k-1}}$, on the current control input, $\mathbf{u_k}$; $\mathbf{w_k}$ is random noise representing the uncertainty of the model. The output function, **h()**, relates the observed variables, $\mathbf{z_k}$, to the current state, $\mathbf{x_k}$; $\mathbf{v_k}$ is the measurement noise.

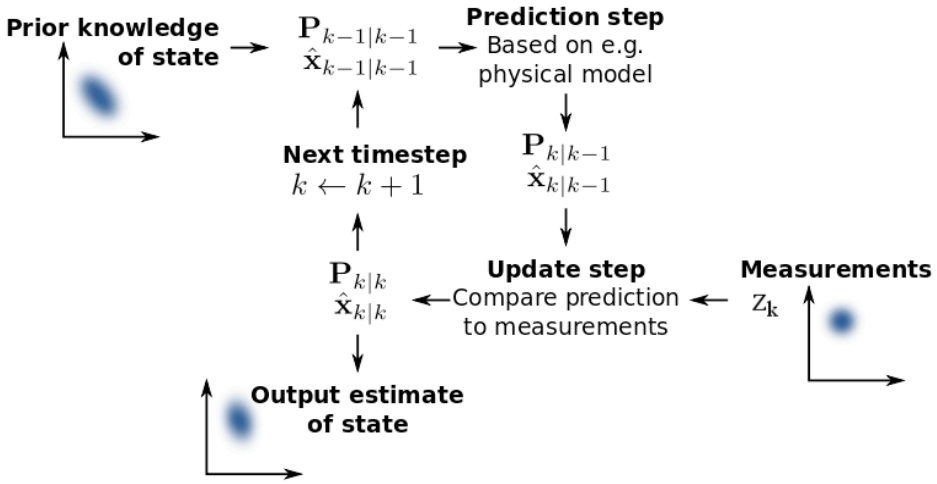

Fig. 3.2 - Standard Kalman Filter iteration. The a priori knowledge of the state (mean and covariance) evolves in time according to a physical model of the process to be observed (prediction step). A prediction of the observed variable is also generated and compared to actual measurements to compute the "sensor residual error". The error is then used to correct mean and covariance of the state estimate (update step) and start again the iteration.

Chapter 3. Sensor fusion

As already pointed out in §3.1, the KF is an algorithm that uses a series of measurements observed over time, containing noise and other inaccuracies, and produces estimates of unknown variables that represent the state of the dynamical system under examination (see Fig. 3.2).

More formally, the KF operates recursively on streams of noisy input data to produce a statistically optimal estimate of the underlying system state. The KF theory assumes that the underlying system is a linear dynamical system and that all error terms and measurements have a Gaussian distribution. Given a generic dynamical system, whose state equations are non-linear (eq. 1), the Kalman Filter can only be applied in a modified version, either the Extended Kalman Filter (EKF) or the Unscented Kalman Filter (UKF). The first is based on a first order linearization of the non-linear state equations (**f()** and/or **g()**): the standard KF is then applied using the Jacobians of the non linear functions. The UKF represents a derivative-free (no need for computationally expensive calculation of Jacobian and Hessian), alternative to the EKF, and builds on the principle that it is easier to approximate a Gaussian distribution than it is to approximate an arbitrary nonlinear function. In the UKF an approximation of the non-linear distributions is estimated using a deterministic sampling algorithm called *Unscented Transform* (UT) (Julier 2002).

The Unscented Transform (UT) is a method of predicting the mean and covariance of a random variable, x, which undergoes a non-linear transformation, y=f(x). The method is based on a deterministic sampling to extract a set, S, of points, X_i, (the "sigma points") from the random variable *x* and associated weights, W_i:

$$S = \{W_i, X_i\} \qquad \text{where } \sum_i W_i = 1 \tag{3.2}$$

The UT allows us to easily compute the mean, $\overline{y}$, and the covariance, P_{yy}, of the transformed variable, *y*, starting from the transformed set of sigma points $Y_i = f(X_i)$, as follows:

$$\bar{y} = \sum_i W_i Y_i$$
$$P_{yy} = \sum_i W_i \left(Y_i - \bar{y}\right)\left(Y_i - \bar{y}\right)^T \quad (3.3)$$

Julier and Uhlmann (2004) proved that these estimates are accurate up to the second order of the Taylor series expansion of f(x).

3.3 UKF-based sensor fusion for robust tracking in surgical navigation

3.3.1 Background

Navigation systems are being used in technologically advanced surgical platforms in order to improve the outcome of procedures such as orthopedic surgery (De Momi et al., 2009), abdominal surgery (Zhang et al., 2006), neurosurgery (Grunert et al., 2003) and others. Navigation platforms consist of a) a localization system for tracking the position and orientation of patient body parts and surgical instruments; b) a central computer for managing the data acquisition stream, and for registering the data to preoperative images, typically Magnetic Resonance Imaging (MRI) or Computed Tomography (CT) scans; and c) a display for visualization. A plethora of different sensing technologies have been introduced into the OR during the past two decades, with the purpose of improving the accuracy and safety of surgical procedures for both patients and operators (Taylor and Stoianovici, 2003), (Beasley and Howe, 2009), (Haidegger et al., 2008).

Among the variety of sensors used in the OR (Vaccarella et al., 2012b), optical localization systems (OTS) (typically near-infrared cameras, which localize active or passive markers) are the most widespread for surgical navigation due to their accuracy, ease of use, and cost-effectiveness (Joskowicz and Taylor, 2001). However, OTS requires clear line-of-sight (Halvorsen et al., 2005), which is difficult to ensure in current overcrowded ORs. When a prolonged marker occlusion occurs, proper visual/audio feedback should be provided to alert the surgeon. In cases of short-term occlusion (e.g. medical professionals passing through the working volume of the camera), the absence of sensor data will result in a flickering effect of the tracked object on the screen. To address this line-of-sight problem in optical

trackers, different approaches have been proposed. The first common method increases the visibility of the tracked object; for example, with a multi-surface markerization (Fürtjes et al., 2011). While this method increases the visibility of the object with different orientations in space, it does not solve the line-of-sight issue due to camera occlusion. The second approach is a state space approach based on different implementations of the Kalman filter. This technique is frequently used to solve robust pose estimation problems (Halvorsen et al., 2005), (Simpson et al., 2007), (Vaccarella et al., 2012a).

Simpson et al. (2007), proposed an Unscented Kalman Filter (UKF) to estimate the uncertainty in localizing the pose of a surgical instrument based on optical markers measurements. The main limitation of this work is the Euler angles representation of the rigid body rotation, which introduces kinematic singularities. Halvorsen et al. (2005) proposed an Extended Kalman Filter (EKF) based on noisy marker measurements to estimate the rigid body pose with application to human motion analysis. The filter shows good performance in also managing marker visibility occlusion; however, the main limitation is the adopted parameterization of rigid body motion (cardanic linkage and helical axis), which suffers from kinematic singularities as well. In Vaccarella et al. (2012a), a quaternion-based UKF was used to estimate translation and rotation of an optically tracked surgical tool in cases of short line-of-sight occlusions. The filter is based on a first order model and showed a maximum error of 2.5 degrees for rotation and 2.36 mm for translation in cases of occlusion lasting for 10 samples (20Hz acquisition rate).

Whereas optical trackers are widely used for tracking instruments in open surgery, their application is very limited in laparoscopic surgeries where procedures are carried out through a small access to the target organ. In these procedures, flexible probes are needed to be tracked from inside the patient body (Ko et al., 2011). In such applications, EMTS are widely used (Cleary et al., 2005b). With the recent advancement in miniaturization of the sensor, EMTS are being predominantly used in a variety of medical applications (Krücker et al., 2007), (Wood et al., 2005), (Nijmeh et al., 2005),

(Yoon et al., 2006). These systems are not subject to the clear line-of-sight limitation, but are less accurate and suffer from magnetic field distortion in the presence of metal objects or electrically powered devices (e.g. operating tables, drills, robots, etc.) (Zhang et al., 2006), (Frantz et al., 2003). Nafis et al. (2006) showed, in fact, that metal objects can affect the performance of commercially available EMTS with errors up to 27 mm.

Another common drawback of most tracking systems is a relatively low update rate which, for example, compromises their application for controlling a robot during contact tasks. A common method used to enhance tracking performance is to include inertial measurements of the object to be localized. IMUs provide information on linear acceleration and angular velocity of a rigid body at a high frame rate (up to 1 kHz), but suffer from integration drift if used to measure translation and rotation. Tracking systems can be integrated with IMUs to overcome limitations such as occluded line-of-sight (OTS), electromagnetic distortion (EMTS), low frame rate (both OTS and EMTS), and integration drift (IMU). In Tobergte et al. (2009), optical and inertial data are fed into a model-based data fusion algorithm, using an EKF for application to robotic surgery for patient motion compensation. Roetenberg et al. (2007) used a Kalman Filter to combine an IMU with a wearable EMTS for human motion analysis. Similarly, Ren et al. (2012) combined inertial and electromagnetic tracking data for the localization of a surgical tool using an EKF.

Chung et al. (2004), improved EMTS accuracy in image-guided surgery applications using optical measurements as a gold standard; EMTS and OTS reference systems are registered once with a calibration procedure, and the pre-computed electromagnetic field distortion correction is then applied to all the EMTS measurements in the OR. Recently, a combined use of EMTS and OTS also found successful application in navigated laparoscopic ultrasonography (LUS), a technique used to acquire intra-body ultrasound images, typically of the liver and pancreas (Feuerstein et al., 2007). Similarly to Chung et al. (2004), Feuerstein et al. (2007) used an OTS to correct EM field distortion; in this case, the correction was not pre-computed, but continuously updated through the hybrid magneto-optical tracking of a

flexible laparoscope ultrasound transducer. However, no probabilistic approach was used to fuse optical and electromagnetic data together, and line-of-sight occlusions were not taken into account.

Data synchronization in sensor fusion is a particularly challenging task. In order to obtain precise synchronization, a sufficiently accurate global timing for all sensors is necessary (Kaempchen and Dietmayer, 2003). In this respect, different protocols were defined for the sensor network, such as the Network Time Protocol (NTP) (De Vito et al., 2008) and the Precision Time Protocol (PTP) (Na et al., 2007). As discussed in Chapter 2 and published in Vaccarella et al. (2012b), a centralized approach for data acquisition can be adopted, where a single module acquires data from all sensors and time-stamps it with a unique clock and broadcasting information in a client-server network.

In this work, robust tracking of surgical instruments during navigated surgery is achieved using a sensor fusion algorithm that allows for overcoming the limitations of the two adopted localization systems, OTS and EMTS. The proposed algorithm uses the UKF, which makes use of a deterministic sampling to estimate the probability distribution of random variables undergoing a non-linear transformation, rather than approximating the non-linear functions (see §3.2). Data acquisition and synchronization is based on the SM architecture presented in Chapter 2. The sensor fusion approach was compared with the UKF-based prediction of instrument pose without using data from the EMTS, as in Vaccarella et al. (2012a). We demonstrate that it is possible to compensate for short marker occlusion (9 samples), providing a continuous estimate of the instrument pose with clinically acceptable accuracy. Furthermore, the proposed algorithm proves to increase the accuracy of EMTS in the presence of magnetic field distortion.

3.3.2 Materials and methods

Spatial transformations and system calibration

OTS and EMTS refer their measurements to their internal reference frame. In Fig. 3.3, the surgical instrument is represented as a triangle with three optical markers on the vertices, and with a six degrees of freedom (DoFs)

sensing coil in the center. Coordinate frames and their spatial relationships are also shown in Fig. 3.3, and the following notation is adopted:

Reference Frames (RF) are associated to tracking systems' internal coordinate systems;

Dynamic Reference Frames (DRF) are associated with tracked objects and will be referred to as optical (ODRF) or electromagnetic (EMDRF), depending on the adopted tracking system; the spatial transformation from reference frame A to B is denoted as ${}^{A}T_{B}$.

The setup depicted in Fig. 3.3 includes the following reference frames:

- **RF_{OTS}**: the OTS internal reference frame. All optical measurements are referred to this reference frame.
- **RF_{EMTS}**: the EMTS internal reference frame. All electromagnetic measurements are referred to this reference frame.
- **ODRF_EMTS**: the DRF associated to optical markers on the EM field generator.
- **ODRF_target**: the DRF associated to optical markers on the target object (e.g. the surgical instrument). Estimating the pose of this reference frame is the objective of this work.
- **EMDRF_target**: the DRF associated to a sensing coil on the target object.

For a combined use of information from sensors acquiring optical and electromagnetic poses within a sensor fusion framework, the spatial relationship between the OTS and EMTS internal reference system must be known. This means to estimate the *X* and *Y* matrices (see Fig. 3.3) with a calibration procedure, solving the following system of equations:

$$A \cdot X = Y \cdot B \tag{3.4}$$

where:

$$\begin{cases} A = {}^{\text{ODRF\_EMTS}}T_{\text{ODRF\_target}} = {}^{\text{OTS}}T^{-1}_{\text{ODRF\_EMTS}} \cdot {}^{OTS}T_{\text{ODRF\_target}} \\ B = {}^{\text{EMTS}}T^{-1}_{\text{EMDRF\_target}} \end{cases} \tag{3.5}$$

where all the spatial transformations are depicted in Fig. 3.3

Equation (3.4) was solved with an iterative approach, as described in De Momi et al. (2008), employing a set of 30 acquired poses spanning the entire measurement volume of the EMTS.

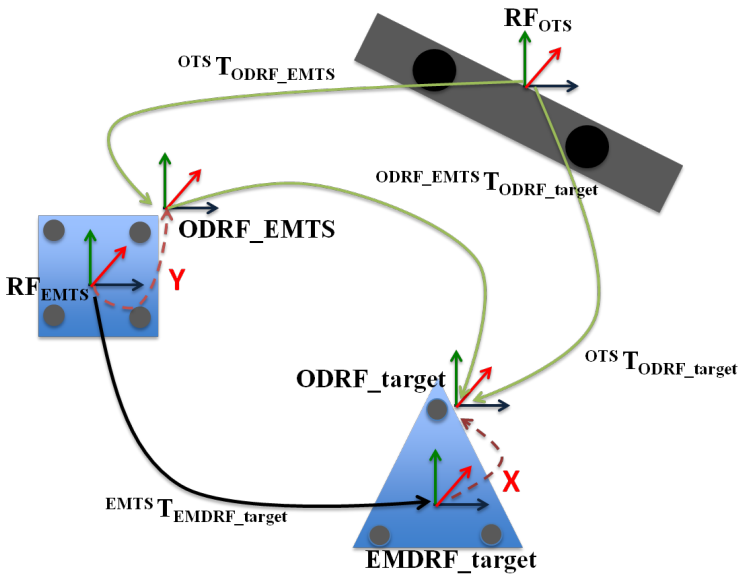

Fig. 3.3 - Spatial relationships involved in system calibration. The presented coordinate systems are the following: RF_{OTS}, OTS internal reference frame; RF_{EMTS}, EMTS internal reference frame; ODRF_EMTS, DRF associated to optical markers on the EM field generator; ODRF_target, DRF associated with optical markers on the target object; EMDRF_target, DRF associated to a sensing coil on the target object. OTS and EMTS refer the measurements to their internal reference system: calibration matrices X and Y are needed to represent data from one system in the reference frame of the other.

UKF is a powerful tool-finding application in fields ranging from measurement uncertainty evaluation (Angrisani et al., 2006) to image processing (Ijaz et al., 2008), motion estimation of hidden body segment (De Momi et al., 2012), and multiple sensor fusion (Yang and Zhang, 2005). Similarly to standard Kalman Filters, UKF provides state estimation based on measurements, process model, and measurement model; this is done in two steps: prediction and update.

Process Model

A constant velocity (both linear and angular) model, also referred to as Continuous White Noise Acceleration Model (CWNA) (Bar-Shalom et al., 2001), (Cerveri et al., 2003), was used to describe the motion of the surgical instrument, including linear and angular velocities in the state vector, even though the rotation is represented with a unit quaternion. The state vector is

shown in (3.6), where $\boldsymbol{p}$ [1x3] is the translation vector (Cartesian coordinates); $\boldsymbol{v}$ [1x3] is the linear velocity vector; $\boldsymbol{q}$ [1x4] is the quaternion describing the orientation of the surgical instrument; and $\boldsymbol{\omega}$ is the angular velocity vector.

$$\boldsymbol{x} = \begin{bmatrix} \boldsymbol{p} & \boldsymbol{v} & \boldsymbol{q} & \boldsymbol{\omega} \end{bmatrix}^T \tag{3.6}$$

The quaternion representation for describing the orientation was chosen in order to avoid kinematic singularities of conventional Euler Angles parameterizations. The state vector evolves in time according to the chosen process model, i.e. constant velocity model; see (3.11). The term to update the position is straightforward and is given by the linear velocity vector times the time interval. In regards to the orientation, the term to update the current attitude is given by the angular velocity times the time interval; this results in a rotation vector, which expresses the orientation in terms of an axis, represented by a unit vector $\boldsymbol{u}$ in Cartesian space, and an angle, $\boldsymbol{\theta}$, of rotation around the same axis, $\boldsymbol{u}$ (see Appendix A). As shown in (3.7) and (3.8), we take advantage of the exponential/logarithmic mapping between a quaternion, $\boldsymbol{q}$, and a rotation vector, $\boldsymbol{r}$ (Grassia, 1998):

$$\boldsymbol{r} = \boldsymbol{\theta} \cdot \boldsymbol{u} \tag{3.7}$$

$$\boldsymbol{q} = \mathrm{e}^{\boldsymbol{r}} \quad \text{and} \quad \boldsymbol{r} = \ln(\boldsymbol{q}) \tag{3.8}$$

Thus, we derive the update equation for the quaternion, given the angular velocity vector, $\boldsymbol{\omega}$, and a time interval, $\boldsymbol{dt}$, considering the differential rotation as follows:

$$\mathrm{d}\boldsymbol{q} = \mathrm{e}^{\boldsymbol{\omega}\mathrm{dt}} \tag{3.9}$$

Similarly to Kraft (2003), the process noise, $\boldsymbol{w}$, is expressed in terms of degrees of freedom of the state vector, regardless the actual dimension of the

state vector (13, due to the quaternion representation). Thus, the noise vector is 12-dimensional:

$$\boldsymbol{w} = \begin{bmatrix} \boldsymbol{w}^{p} & \boldsymbol{w}^{v} & \boldsymbol{w}^{\alpha,\beta,\gamma} & \boldsymbol{w}^{\omega} \end{bmatrix}^{T} \tag{3.10}$$

where $\boldsymbol{w}^{p}$ represents the noise on the translation vector; $\boldsymbol{w}^{v}$ represents the noise on the linear velocity vector; $\boldsymbol{w}^{\alpha,\beta,\gamma}$ represents the noise on the rotation expressed by three components (noise on rotations around the three axis x, y, z); and $\boldsymbol{w}^{\omega}$ represents the noise on the angular velocity. Consequently, the noise vector cannot be simply added to the state vector; the rotation noise vector, $\boldsymbol{w}^{\alpha,\beta,\gamma}$, has to be converted in the corresponding noise quaternion $\boldsymbol{q}^{w}$, according to (3.8), and multiplied by the quaternion representing the current rotation.

The covariance matrix of the process noise, $\boldsymbol{Q}$, is defined as described by Fioretti (1996). According to the dimension of the noise vector, $\boldsymbol{w}$, $\boldsymbol{Q}$ is a 12-by-12 matrix. The state transition function (3.11), which describes the evolution of the state from time *k* to time *k+1*, is non-linear since the four components of the quaternion need to be updated starting from the three angular velocities:

$$\boldsymbol{f}\left(\boldsymbol{x}_k,\ \boldsymbol{w}_k,\ \mathrm{dt}\right) = \boldsymbol{x}_{k+1} = \begin{bmatrix} \boldsymbol{p}_k + \boldsymbol{v}_k \cdot \mathrm{dt} + \boldsymbol{w}_k^{p} \\ \boldsymbol{v}_k + \boldsymbol{w}_k^{v} \\ \boldsymbol{q}_k \cdot \boldsymbol{q}_k^{w} \cdot \mathrm{d}\boldsymbol{q} \\ \boldsymbol{\omega}_k + \boldsymbol{w}_k^{\omega} \end{bmatrix} \tag{3.11}$$

where dt is the time step of the filter.

Measurement Model

The output function, h, relates the current estimate of the state vector, $\hat{\boldsymbol{x}}_{\mathrm{k}}$ with the measured variables, $\boldsymbol{z}_{\mathrm{k}} = \mathrm{g}\left(\boldsymbol{x}_{\mathrm{k}},\ \boldsymbol{\nu}_{\mathrm{k}}\right)$, in presence of white Gaussian noise, $\boldsymbol{\nu}_{\mathrm{k}}$, whose covariance matrix, **R**, depends on measurement accuracy:

$$\boldsymbol{\nu} \sim N(0,\boldsymbol{R}), \quad \boldsymbol{R} = \begin{bmatrix} \boldsymbol{R}_{m1} & 0 & 0 & 0 \\ 0 & \boldsymbol{R}_{m2} & 0 & 0 \\ 0 & 0 & \dots & 0 \\ 0 & 0 & 0 & \boldsymbol{R}_{mN} \end{bmatrix} \tag{3.12}$$

where R_{mi} expresses the measurement uncertainty of the i-th (i=1…N) optical marker:

$$\boldsymbol{R}_{mi} = \begin{bmatrix} a_x^2 & 0 & 0 \\ 0 & a_y^2 & 0 \\ 0 & 0 & a_z^2 \end{bmatrix} \tag{3.13}$$

where a_x, a_y and a_z are the vendor's stated accuracies on the three axis. $\boldsymbol{R}$ is set as diagonal matrix since marker measurements are considered independent from each other; furthermore, the sub-matrices $\boldsymbol{R}_{mi}$ are also diagonal as the error in determining each marker coordinate (e.g. x), due to the other two (e.g. y and z), is considered to be negligible.

In the proposed model, the measured variables are the 3D position of each marker fixed to the target rigid body, thus the output vector will be a 3L-dimensional vector, where L is the number of markers.

The configuration of the markers and their position, with respect to the rigid body reference frame, is fixed and known, ${}^{\text{ODRF\_target}}\boldsymbol{p}_{m_i}$, and is stored in the matrix M in homogenous coordinates (in case of three markers):

$$\boldsymbol{M} = \begin{bmatrix} {}^{\text{ODRF\_target}}\boldsymbol{p}_{m1} & {}^{\text{ODRF\_target}}\boldsymbol{p}_{m2} & {}^{\text{ODRF\_target}}\boldsymbol{p}_{m3} \\ 1 & 1 & 1 \end{bmatrix} \tag{3.14}$$

The estimated absolute position (with respect to the localization system) of each marker is:

$$\hat{\boldsymbol{z}}_{\mathrm{k}} = \mathrm{h}\left(\hat{\boldsymbol{x}}_{\mathrm{k}}, \boldsymbol{v}_{\mathrm{k}}\right) = \begin{bmatrix} \mathrm{Rot}\left(\hat{\boldsymbol{q}}_{\mathrm{k}}\right) & \hat{\boldsymbol{p}}_{\mathrm{k}} \\ 0 & 1 \end{bmatrix} \cdot \boldsymbol{M} + \boldsymbol{v}_{\mathrm{k}} = {}^{\mathrm{OTS}}\hat{\boldsymbol{T}}_{\mathrm{ODRF\_target}} \cdot \boldsymbol{M} + \boldsymbol{v}_{\mathrm{k}} \qquad (3.15)$$

where $\mathrm{Rot}\left(\hat{\boldsymbol{q}}_{\mathrm{k}}\right)$ is the rotation matrix associated to the quaternion $\hat{\boldsymbol{q}}_{\mathrm{k}}$, and ${}^{OTS}\hat{T}_{ODRF\_\mathrm{target}}$ is the 4x4 transformation matrix of the rigid body associated with the current estimate of the state. The filter recursively corrects the current state estimate based on the difference between the expected position of the markers, $\hat{\boldsymbol{z}}_{\mathrm{k}}$, and the actual measured data, $\boldsymbol{z}_{\mathrm{k}}$, which is commonly referred to as the innovation vector of the filter.

Marker Occlusion

In cases where there is no data for one or more optical markers available (e.g. in case of line-of-sight occlusion), the proposed Sensor Fusion (SF) algorithm uses data from the EMTS to supply the missing optical data. Results were compared with the algorithm described in a previous work (Vaccarella et al., 2012a), which relies only on the system model and on the available measurements. We will refer to the latter as the No Sensor Fusion algorithm (NSF).

Each optical marker position in the OTS coordinate system can be estimated from an EMTS measurement, as shown in Fig. 3.4. As an example, if marker m1 (as in Fig. 3.4) is not visible, its position can be retrieved as follows:

$${}^{\mathrm{OTS}}\boldsymbol{p}_{\mathrm{m1}} = {}^{\mathrm{OTS}}\boldsymbol{T}_{\mathrm{ODRF\_EMTS}} \cdot \boldsymbol{Y}^{-1} \cdot {}^{\mathrm{EMTS}}\boldsymbol{T}_{\mathrm{EMDRF\_target}} \cdot \boldsymbol{X} \cdot {}^{\mathrm{ODRF\_target}}\boldsymbol{p}_{\mathrm{m1}} \qquad (3.16)$$

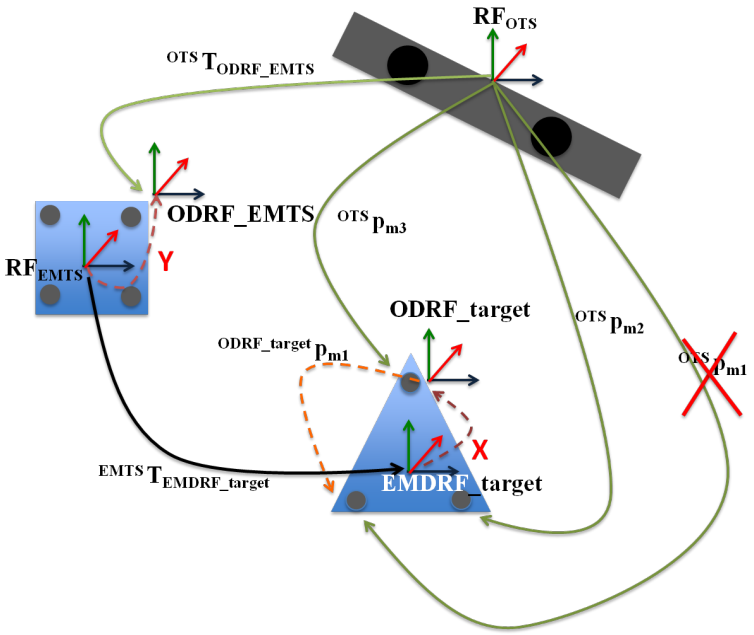

Fig. 3.4 - EMTS measurements are used in cases of marker occlusion to estimate the position of the missing marker in the OTS reference system. For simplicity, only $^{ODRF\_target}p_{mi}$ is shown. The other coordinate systems in the figure are the following: RF_{OTS}, OTS internal reference frame; RF_{EMTS}, EMTS internal reference frame; ODRF_EMTS, DRF associated to optical markers on the EM field generator; ODRF_target, DRF associated with optical markers on the target object; EMDRF_target, DRF associated to a sensing coil on the target object.

In the presented setup, the optical markers' position derived from EMTS measurement is subject to calibration inaccuracy, and in the presence of metal or electrically powered objects, measurement errors in localizing the coil can occur due to magnetic field distortion. As a consequence, an error transformation matrix, ***E***, relates the estimated pose to the actual pose of the target.

The error matrix ***E*** (see Fig. 3.5), is computed at each acquisition step as follows:

$$\boldsymbol{E} = \left({}^{OTS}\boldsymbol{T}_{ODRF\_EMTS} \cdot \boldsymbol{Y}^{-1} \cdot {}^{EMTS}\boldsymbol{T}_{EMDRF\_target} \cdot \boldsymbol{X} \right)^{-1} \cdot {}^{OTS}\hat{\boldsymbol{T}}_{ODRF\_target} \qquad (3.17)$$

where ${}^{OTS}\hat{\boldsymbol{T}}_{ODRF\_target}$ is the pose of the target as estimated by the UKF.

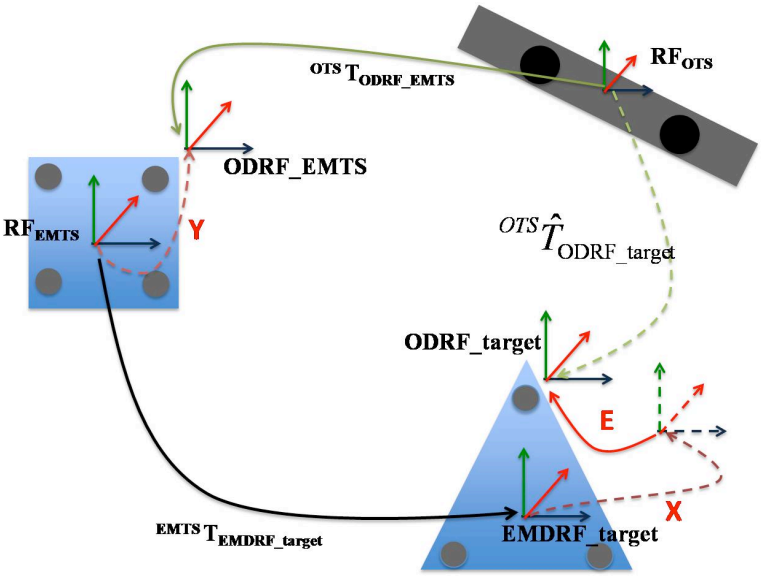

Fig. 3.5 - Distortion correction is achieved by computing matrix E at each filter step and using it to improve the EMTS-based estimate of missing markers. The other coordinate systems in the figure are the following: RF_{OTS}, OTS internal reference frame; RF_{EMTS}, EMTS internal reference frame; ODRF_EMTS, DRF associated to optical markers on the EM field generator; ODRF_target, DRF associated with optical markers on the target object; EMDRF_target, DRF associated to a sensing coil on the target object.

The error matrix is then used in the sensor fusion algorithm when one or more optical markers are missing to further correct the EMTS-based prediction of marker position. Thus equation (3.16) becomes:

$$ {}^{OTS}\boldsymbol{p}_{m1} = {}^{OTS}\boldsymbol{T}_{ODRF\_EMTS} \cdot \boldsymbol{Y}^{-1} \cdot {}^{EMTS}\boldsymbol{T}_{EMDRF\_target} \cdot \boldsymbol{X} \cdot \boldsymbol{E} \cdot {}^{ODRF\_target}\boldsymbol{p}_{m1} \qquad (3.18) $$

The covariance matrix of the measurement noise, $\boldsymbol{R}$, is tuned according to the available measurements. As long as all markers are optically tracked, the stated accuracy of the OTS is used to define the covariance matrix $\boldsymbol{R}$, as shown in (3.12) and (3.13). When one or more optical markers' position are obtained through electromagnetic measurements, the corresponding elements of $\boldsymbol{R}$ are set to a higher value, given by the variance of the calibration residual translation error.

Fig. 3.6 summarizes the main steps of the two algorithms, NSF and SF.

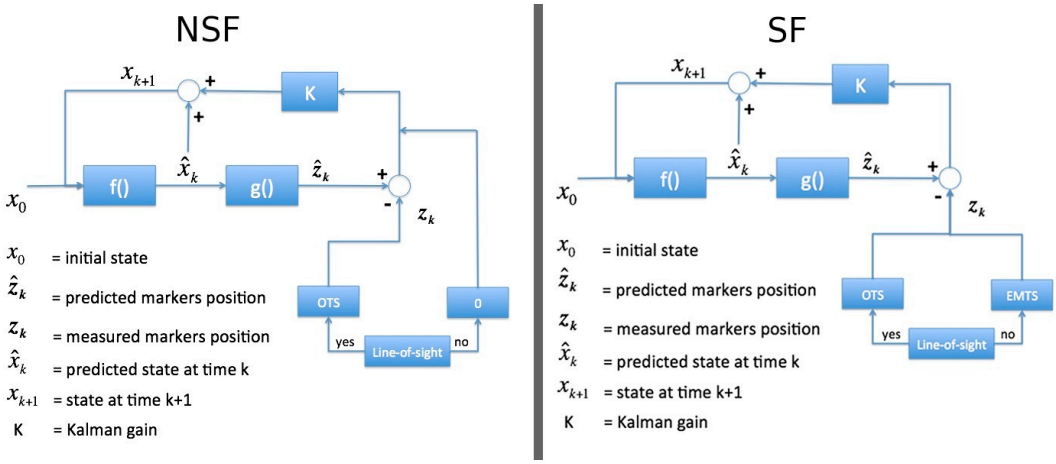

Fig. 3.6 - Block diagram of the two algorithms. The Kalman prediction-update cycle is performed in both algorithms, which have different behaviors in case of optical marker measurement unavailability. As shown on the left side, the NSF algorithm replaces the difference between predicted and actual optical measurements with a vector of zeros. The SF algorithm (right side), on the other hand, always provides a non-zero measurement vector z_k; in cases of line-of-sight occlusion, optical marker positions are indirectly derived by electromagnetic measurement.

Experimental Setup and Protocol

A Polaris Vicra (NDI, Canada) and Aurora (NDI, Canada) systems were used for OTS and EMTS respectively. A six DoFs EM sensor was attached to a three-markers optical pointer, as shown in Fig. 3.7.

The centralized module for data acquisition and time-stamping, described in Chapter 2, was used as a server in a distributed architecture over the TAO-Corba protocol.

The calibration matrices **X** and **Y**, as in (3.4), were estimated by recording 30 static poses with both OTS and EMTS. The residual translation error was evaluated using the norm of the translation vector of the transformation matrix, ***E*** computed as in (3.17); whereas the residual rotation error was computed as the norm of the Euler angles extracted from the rotation part of ***E***. Median residual calibration errors and the inter-quartile range were computed.

After the calibration procedure, two experiments were carried out. Experiment #1 was aimed at comparing the SF and NSF algorithm in cases of line-of-sight occlusion of approximately one and two seconds (9 and 19 samples), which are comparable with a possible line-of-sight occlusion due to a surgeon accidentally hiding the markers during the surgery. Experiment #2

was aimed at evaluating the performance of the SF algorithm in the presence of magnetic field distortions.

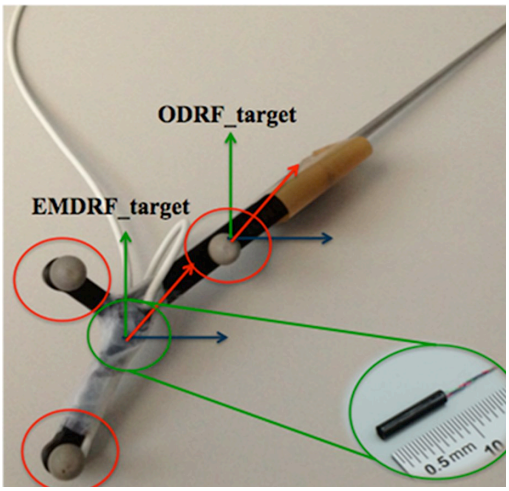

Fig. 3.7 - Hybrid pointer localized by means of three retroreflective optical markers, circled in red, and of a sensing coil, marked in the green circle. The dynamic reference frame (DRF) associated with the three optical markers is denoted with ODRF_target, while the DRF associated with the electromagnetic sensing coil is denoted with EMDRF_target.

Experiment #1

In order to compare the SF and NSF algorithm performances, a set of 30 trajectories was used. The pointer was moved freehand for 30 seconds and the motion was sampled with both tracking systems at 10 Hz. The following groups of trajectories were identified:

- 3 arcs
- 3 circles
- 7 curve lines
- 5 straight lines
- 3 eight-shaped path
- 3 random
- 3 rectangles
- 3 sinusoids

Marker occlusions were simulated. The optical measurements of the pose of the optical DRF attached to the pointer, ${}^{OTS}\boldsymbol{T}_{ODRF\_target}$, during the entire acquisition were used as references for error computation.

As shown in Fig. 3.8, an occlusion window lasting 9 samples was applied N times (N = 27), shifting it over the entire acquisition and hiding 1, 2, and all 3 markers.

To evaluate the performance of the algorithm as functions of the occlusion duration, the same protocol is also adopted for N=13 occlusion windows lasting 19 samples.

Details of the experimental protocol are summarized in Table 3.1

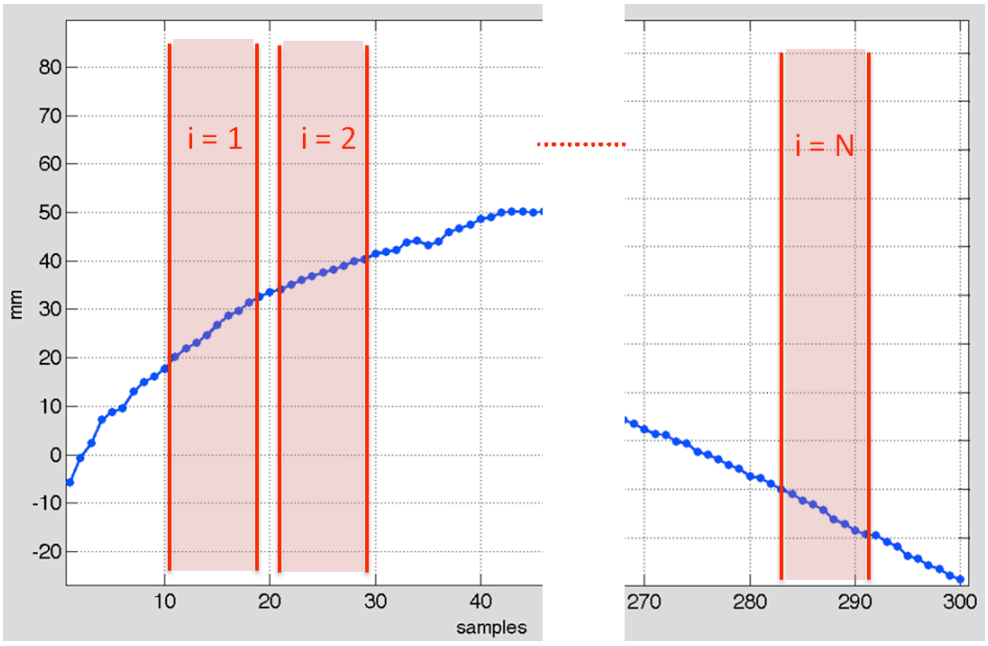

Fig. 3.8 - Example of motion along the x-axis of one optical marker. A nine samples occlusion window has been applied N = 27 times shifting it over the entire acquisition. The process is repeated three times hiding one, two and three markers respectively. The same protocol was also applied to N = 13 occlusion windows lasting 19 samples.

Root Mean Square Error (RMSE) and a 95% Confidence Interval (CI) were computed as functions of the sample lag from the beginning of the occlusion window. The error was computed considering all 30 datasets together and clustering them based on the 3D shape of the trajectory.

Experiment #2

Experiment #2 was designed to test the robustness of the SF algorithm against magnetic field distortion. Chromium-vanadium steel was used as a distorter in the proximity of the EM generator, as shown in Fig. 3.9. As a preliminary step, the static translation accuracy of the EMTS in the aforementioned disturbed environment was evaluated. The sensing coil was held steady in 30 different points of the EMTS working volume. At each point,

the 3D position was recorded at 10 Hz for 20 seconds, with and without metal disturbance. For each point, the average translation vector in the disturbed setup was compared with the average translation vector in the metal-free setup; the norm of the distance between the two was taken as an indicator of the distortion error. RMSE and a 95% confidence interval were computed.

Table 3.1 Experimental protocol

	Experiment #1	**Experiment #2**
Trajectory type	Arcs, circles, curve lines, straight lines, eight-shaped paths, random, rectangles, sinusoids	Curve lines
Number of datasets	30	10
EM distortion	No	Yes
Line-of-sight occlusion	Yes (simulated)	Yes (simulated)
Line-of-sight occlusion length	9 samples	9 samples
	19 samples	
Acquisition freq.	10 Hz	10 Hz
Acquisition length	30 s	30 s
Algorithm	SF, NSF	SF

In the second step of Experiment #2, ten curve line trajectories, in presence of metal objects between the EM field generator and the sensing coil, were acquired to test the SF algorithm's robustness. The quality indicator of the electromagnetic pose data was higher than 2 (NDI suggests discarding all data with a quality indicator higher than 1). Marker occlusion windows were applied with the same protocol as in Experiment #1 and RMSE and a 95% confidence interval were computed.

Details of the experimental protocol are summarized in Table 3.1.

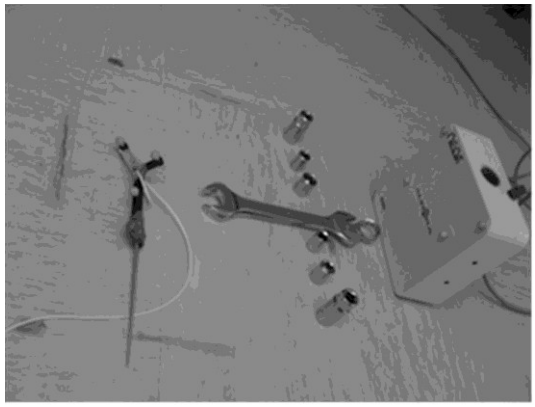

Fig. 3.9 - Metal distorters in the EMTS working volume for static accuracy assessment in high distortion conditions.

3.3.3 Results

System Calibration

Calibration errors were computed on 30 poses, results are summarized in Table 3.2

Table 3.2 - Translation and rotation calibration error: median values are reported together with interquartile values.

Translation error [mm]	Rotation error [deg]
5.89 (3.05 – 7.84)	0.49 (0.28 – 0.9)

Experiment #1

The RMSE for translation and rotation, computed over the entire set of 30 trajectories, are shown in Fig. 3.10, along with a 95% CI, for one, two and three hidden markers. SF results (in grey) are compared to NSF (in black). Errors are shown as functions of the sample lag from the beginning of each occlusion window. Errors increase with the duration of the occlusion, as expected, even though this is less evident in the SF algorithm as compared to NSF. In particular, for the NSF algorithm, the RMSE for translation increases up to 2.8 mm in cases of one hidden marker, 15.3 mm in cases of two hidden markers, and 28.4 mm in cases of complete marker occlusion. Similarly, for the rotation RMSE, NSF shows errors up to 15.3 degrees in cases of one hidden marker, 21.2 degrees in cases of two hidden markers, and 4.7 degrees in cases of complete occlusion. It must be noted that the maximum rotation

error in cases of complete occlusion (Fig. 3.10f) is lower than in case of partial occlusion for the NSF algorithm (Fig. 3.10d-e).

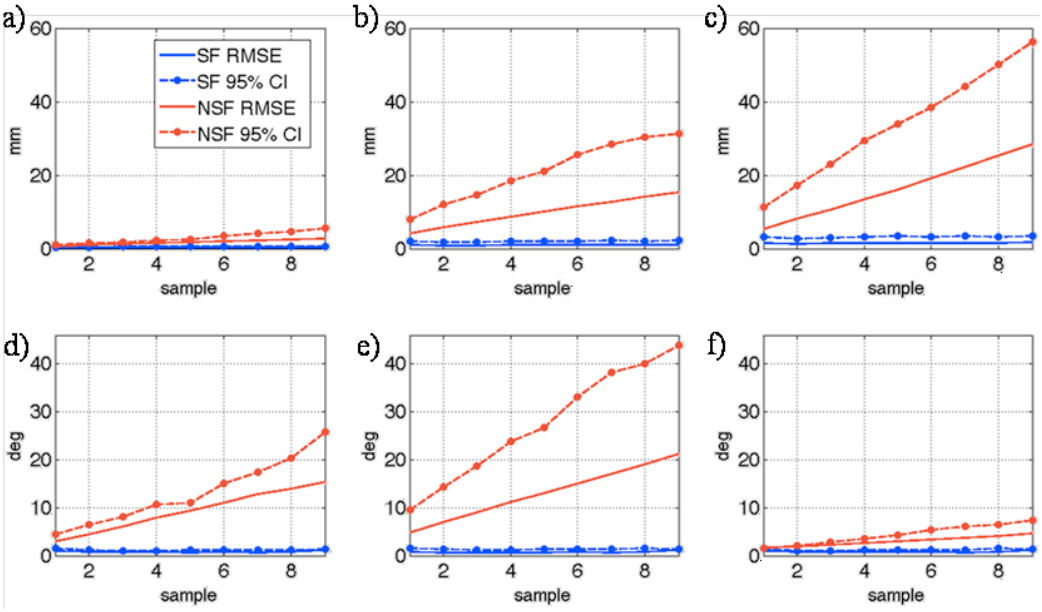

Fig. 3.10 - SF (blue line) compared to NSF (red line) over the entire set of 30 acquisitions. Translation error for 1, 2, and 3 hidden markers are shown in (a), (b), and (c) respectively. Rotation error for 1, 2, and 3 hidden markers are shown in (d), (e), and (f) respectively. Solid lines represent RMSE and dash dot lines the 95% confidence interval computed for each sample of the occlusion window.

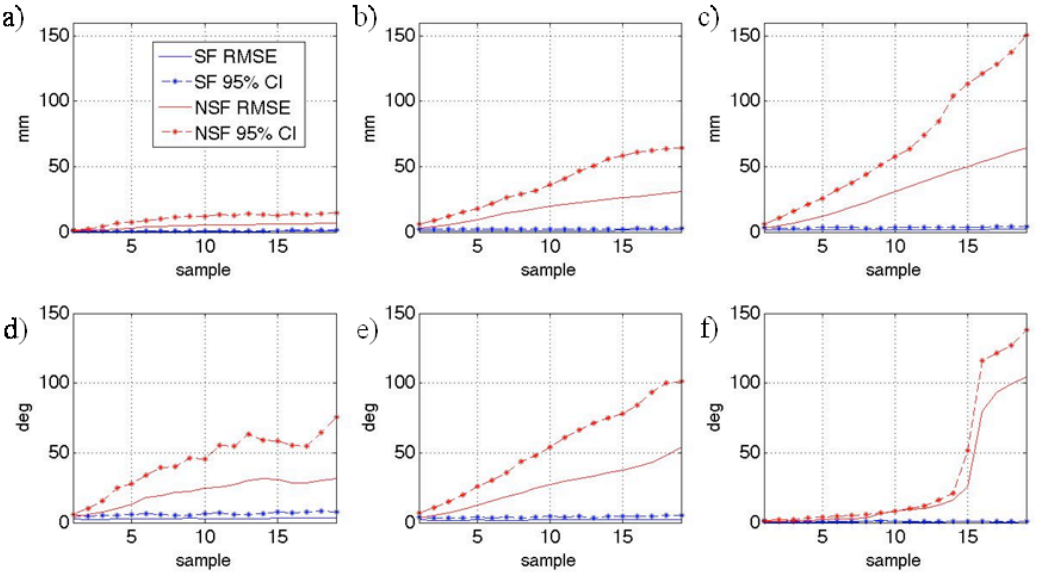

Fig. 3.11 - SF (blue line) compared to NSF (red line) over the entire set of 30 acquisitions on 19 samples occlusion intervals. Translation error for 1, 2, and 3 hidden markers are shown in (a), (b), and (c) respectively. Rotation error for 1, 2, and 3 hidden markers are shown in (d), (e), and (f) respectively. Solid lines represent RMSE and dash dot lines the 95% confidence interval computed for each sample of the occlusion window.

The NSF error dependency on occlusion duration is more evident in Fig. 3.11 where the results for 19 sample occlusion intervals are reported; on the

other hand, the SF algorithm shows a RMS error of less than 2.1 mm for translation and 3.6 deg for rotation. Maximum and minimum translation and rotation RMSE for each type of trajectory are reported, along with the 95% confidence interval in Table 3.3 and Table 3.4 respectively.

Table 3.3 - Minimum and maximum RMSE and 95% CI for translation in the 8 trajectory types for 1, 2, and 3 hidden markers. SF and NSF algorithms are compared.

Trajectory Type	Translation RMSE [mm]				Translation 95% Confidence Interval [mm]			
	SF		NSF		SF		NSF	
	Min	Max	Min	Max	Min	Max	Min	Max
1 Hidden Marker								
Arcs	0.12	0.15	0.17	0.61	0.22	0.28	0.37	1.36
Circles	0.16	0.24	0.23	1.21	0.28	0.44	0.46	2.61
Curve lines	0.22	0.28	0.29	1.25	0.39	0.53	0.55	2.28
Straight lines	0.14	0.19	0.13	0.26	0.23	0.35	0.21	0.52
Eight -shaped	0.23	0.45	0.51	2.24	0.45	1.12	1.19	4.52
Random	0.66	0.81	2.39	9.65	1.16	1.63	4.77	18.0
Rectangles	0.17	0.21	0.20	1.06	0.31	0.44	0.39	1.94
Sinusoids	0.18	0.23	0.29	1.62	0.31	0.47	0.59	2.69
2 Hidden Markers								
Arcs	0.43	0.51	1.49	3.37	0.92	0.73	2.06	5.06
Circles	0.77	0.98	3.25	13.4	1.83	1.35	5.97	27.6
Curve lines	0.99	1.15	3.26	14.6	1.74	2.01	6.31	29.5
Straight lines	0.45	0.62	1.51	2.96	0.71	1.14	2.13	4.41
Eight -shaped	1.19	1.79	7.81	25.9	2.52	3.98	18.1	63.1
Random	1.82	2.15	8.17	31.2	3.07	4.14	13.8	61.7
Rectangles	0.64	0.84	2.47	9.11	1.13	1.78	4.61	23.4
Sinusoids	0.75	0.91	3.05	12.7	1.29	1.65	6.18	22.9
3 Hidden Markers								
Arcs	0.59	0.72	0.81	3.07	0.99	1.35	1.63	6.50
Circles	1.29	1.72	4.11	21.2	2.20	3.30	6.91	37.9
Curve lines	1.48	1.87	4.36	25.0	2.76	3.71	7.85	49.4
Straight lines	0.73	1.03	1.06	3.33	1.32	1.87	2.12	6.87
Eight -shaped	1.88	2.55	10.1	53.6	4.04	5.48	24.4	123
Random	2.43	3.51	11.2	59.4	4.41	7.05	17.4	118
Rectangles	0.99	1.36	2.76	13.6	1.74	3.06	6.02	33.0
Sinusoids	1.19	1.45	3.85	21.3	2.02	2.61	7.34	39.2

Table 3.4 - Minimum and maximum RMSE and 95% CI for rotation in the 8 trajectory types for 1, 2, and 3 hidden markers. SF and NSF algorithms are compared.

Trajectory Type	Rotation RMSE [deg]				Rotation 95% Confidence Interval [deg]			
	SF		NSF		SF		NSF	
	Min	Max	Min	Max	Min	Max	Min	Max
1 Hidden Marker								
Arcs	0.33	0.38	0.60	2.73	0.57	0.79	1.53	6.19
Circles	0.40	0.51	0.64	5.30	0.68	0.82	1.15	11.4
Curve lines	0.47	0.63	1.02	5.51	0.82	1.26	1.93	10.3
Straight lines	0.29	0.37	0.30	1.07	0.48	0.62	0.65	2.06
Eight-shaped	0.46	0.81	1.77	9.87	0.84	1.86	4.02	20.3
Random	2.20	4.37	10.9	54.6	3.63	6.45	108	22.2
Rectangles	0.33	0.43	0.57	4.69	0.60	0.85	1.23	8.69
Sinusoids	0.36	0.47	0.91	7.15	0.63	0.85	1.88	11.7
2 Hidden Markers								
Arcs	0.30	0.35	0.94	3.28	0.47	0.75	1.89	6.06
Circles	0.49	0.61	3.56	17.8	0.82	1.16	7.42	37.9
Curve lines	0.54	0.73	3.74	19.5	1.03	1.33	8.11	40.5
Straight lines	0.28	0.39	0.72	2.27	0.50	0.68	1.64	4.69
Eight-shaped	0.81	1.22	8.89	36.5	1.78	2.71	22.6	85.0
Random	1.52	4.24	10.6	45.3	2.90	4.71	16.2	81.7
Rectangles	0.43	0.56	2.61	11.8	0.78	1.28	4.65	31.1
Sinusoids	0.43	0.59	3.37	17.4	0.79	1.13	6.88	32.1
3 Hidden Markers								
Arcs	0.32	0.41	0.57	1.72	0.60	0.83	0.92	2.82
Circles	0.41	0.53	0.69	2.44	0.74	0.93	1.29	4.26
Curve lines	0.51	0.65	1.07	3.76	0.95	1.35	1.63	7.60
Straight lines	0.31	0.37	0.44	1.26	0.53	0.68	0.68	2.13
Eight-shaped	0.53	0.78	0.99	4.62	1.03	1.80	2.11	11.0
Random	2.02	4.34	5.64	14.6	3.66	6.11	7.57	33.2
Rectangles	0.38	0.46	0.49	1.48	0.70	0.86	0.71	2.19
Sinusoids	0.38	0.49	0.62	2.41	0.75	1.02	1.02	4.77

Fig. 3.12 and Fig. 3.13 show translation and rotation RMSE together with a 95% CI, computed with 1, 2, and 3 hidden markers for arc-shaped and random trajectories respectively. SF results (in blue) are compared to NSF (in red). Errors are shown as functions of the sample lag from the beginning of

the occlusion window. Arc-shaped trajectories showed the lowest amount of error (maximum 3.37 mm for NSF and 0.72 mm for SF), whereas random trajectories the highest (up to 59.4 mm for NSF and 3.5 mm for SF). As in Fig. 3.10, for both arc-shaped and random trajectories, the error increases with the duration of the occlusion and the number of hidden markers; except rotation errors for the NSF algorithm in cases of complete occlusion (Fig. 3.12f and Fig. 3.13f), which is lower as compared to partial occlusion (Fig. 3.12d-e and Fig. 3.13d-e).

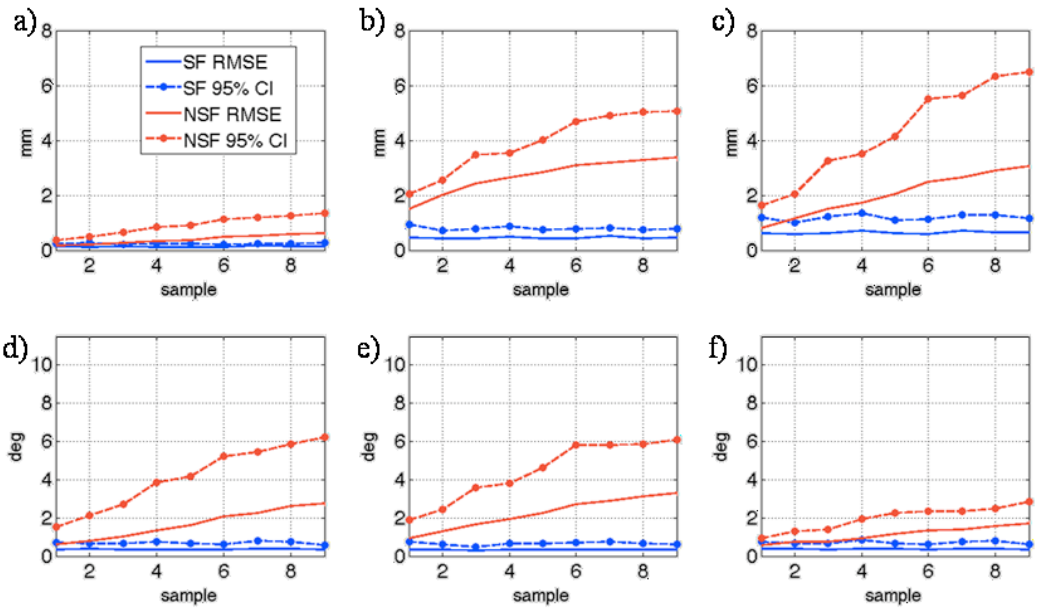

Fig. 3.12 - Translation and rotation error in SF (blue line) compared to NSF (red line) on arch-shaped trajectories. Translation error for 1, 2, and 3 hidden markers are shown in (a), (b), and (c) respectively. Rotation error for 1, 2, and 3 hidden markers are shown in (d), (e), and (f) respectively. Solid lines represent RMSE and dash dot lines the 95% confidence interval computed for each sample of the occlusion window.

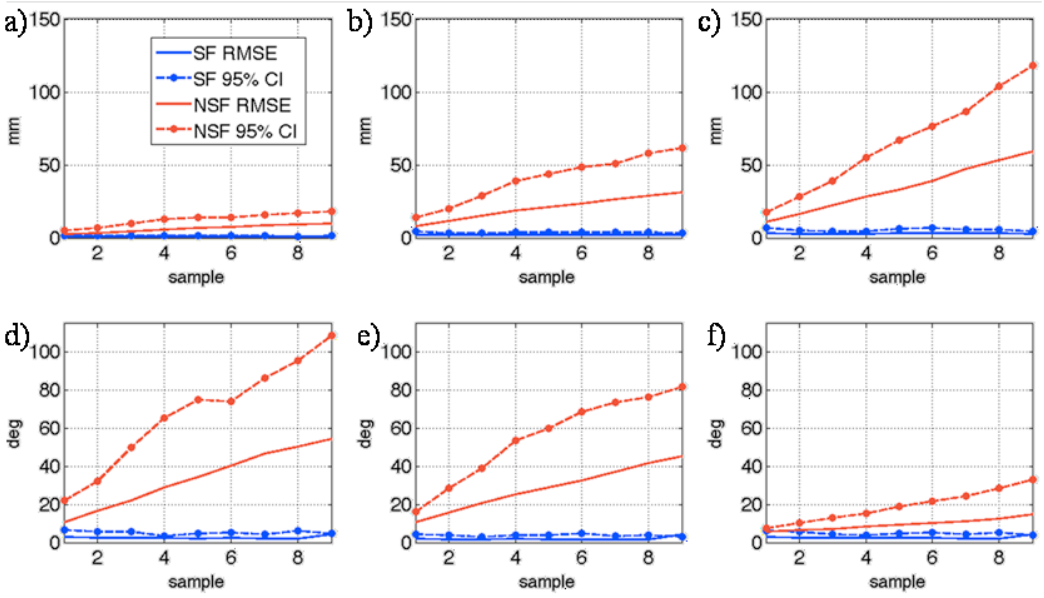

Fig. 3.13 - Translation and rotation error in SF (blue line) compared to NSF (red line) on random trajectories. Translation error for 1, 2, and 3 hidden markers are shown in (a), (b), and (c) respectively. Rotation error for 1, 2, and 3 hidden markers are shown in (d), (e), and (f) respectively. Solid lines represent RMSE and dash dot lines the 95% confidence interval computed for each sample of the occlusion window.

Experiment #2

The static accuracy of the NDI Aurora in the presence of magnetic distortion was experimentally evaluated; RMSE and a 95% confidence interval are reported in Table 3.5, along with the corresponding values in an undisturbed environment, as reported in the vendor's technical specifications (Kirsch, 2005).

Table 3.5 - Static accuracy computed in the disturbed experimental setup, and as reported by the vendor for a metal-free environment.

Static Accuracy - disturbed setup		**Static Accuracy - undisturbed setup** (as reported on NDI technical specifications)	
RMSE	**95% CI**	**RMSE**	**95% CI**
18.64 mm	30.86 mm	1.6 mm	3.0 mm

SF results are shown in Fig. 3.14. Translation RMSE and a 95% confidence interval are computed for 1, 2, and 3 hidden markers over the entire set of 10 acquisitions in a metal-disturbed environment. Errors are shown as functions of the sample lag from the beginning of each occlusion window. The RMSE

ranges from 0.5 mm in cases of partial occlusion, to 3.5 mm in cases of complete occlusion.

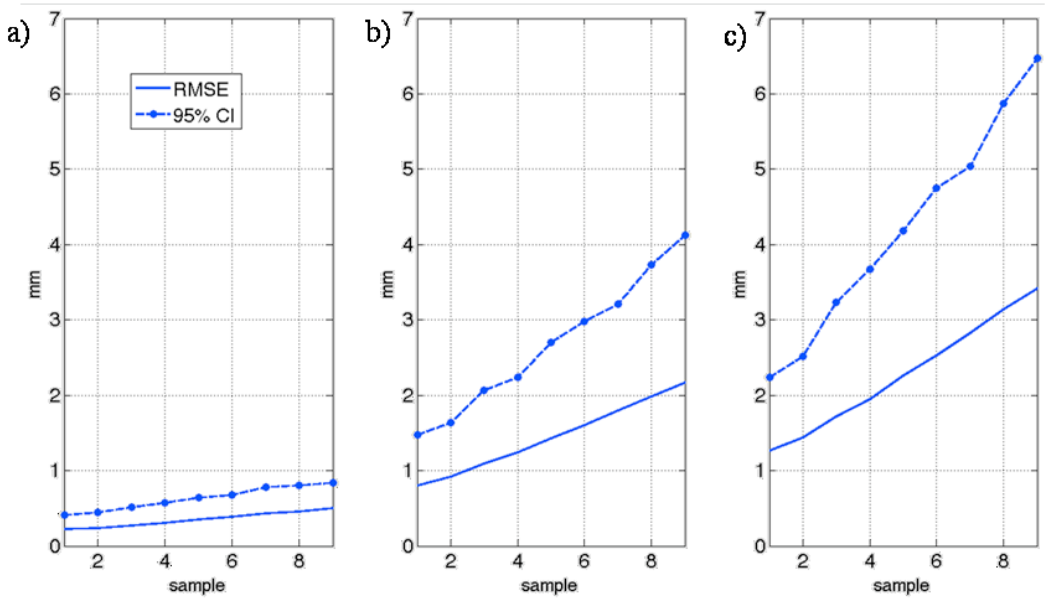

Fig. 3.14 - SF results in cases of metal distortion for 1 (a), 2 (b), and 3 (c) hidden markers. RMSE and a 95% CI are reported.

3.3.4 Discussion

Optical and electromagnetic tracking are two common technologies exploited in surgical navigation systems to localize instruments and the patient's body in the OR. Nevertheless, OTS reliability is limited by line-of-sight requirements and EMTS accuracy is greatly affected by electromagnetic field distortion.

In this chapter, we proposed a Sensor Fusion algorithm (SF) for a combined use of OTS and EMTS data to compensate for both the aforementioned flaws.

A correct temporal alignment of sensor information is essential for guaranteeing the consistency of the fusion algorithm, since wrong data synchronization can be a source of noticeable errors. Data acquisition and synchronization is achieved in our setup with the centralized architecture described in Chapter 2, which ensures a synchronization error within the frequency tolerance of one single quartz crystal oscillator (typically ±10-100 ppm).

In this work, we used UKF to manage non-additive noise required by the quaternion parameterization, and to deal with non-linear functions without

the need of Jacobian computation, as required in EKF. The equations describing the motion of the rigid body rely on quaternion parameterization for rotations and are highly non-linear. Quaternion representation has the advantage of avoiding kinematic singularities, which occur at certain values of rotation angles with other parameterizations, such has cardanic linkage or helical axis (Halvorsen et al., 2005).

Experiment #1 was aimed at evaluating the tracking algorithm robustness to missing measurements (optical markers occlusion) for approximately one two second (9, 19 samples) intervals. The proposed SF algorithm was compared with a UKF-based prediction of the instrument pose, NSF, as reported in (Vaccarella et al., 2012a). Results showed a significant improvement in translation and rotation error when exploiting EMTS data with the SF method. In both the SF and NSF algorithms, the first order model of the filter is a good approximation only in a neighborhood of the occlusion event; thus, the errors increase with the duration of the occlusion if the trajectory deviates from a straight line and constant velocity. However, even in case of longer occlusion intervals (approximately 2 seconds), this is less evident in the SF algorithm, in which the pose estimate is always corrected with a full set of marker measurements. This is a remarkable result since the proposed SF algorithm improves one of the main limitations of the NSF algorithm: the length of the occlusion event. As expected, the translation error also increases the number of hidden markers. This is due to missing measurements in the NSF algorithm and to less accurate measurements in the SF approach. This is not true for the NSF rotation error, as shown in Fig. 3.10d-e-f, where the error in case of complete occlusion is lower than the errors associated with less occluded situations. A possible explanation is that in cases of partial occlusion, the constraint of rigid motion does not hold since missing markers evolve following the first order model, whereas the others are updated according to the measurements. Complete random trajectories showed the worst performance, both for SF and NSF algorithms, and again this is referable to the underlying first order model. On the contrary, on arcs and straight line trajectories, both algorithms perform better and SF showed a tracking error often even lower than the EMTS stated

accuracy (1.2 mm RMSE, 3.0 mm 95% CI) in an environment free of EM distortion. Compared with the EKF-based approach to addressing line-of-sight occlusion proposed by Halvorsen et al. (2005), the presented algorithm shows significantly improved results. Halvorsen et al. (2005), reported translation errors only for partial occlusions of 10 sample intervals, with values varying from 5 to 10 mm.

A remarkable result of the SF algorithm is the accuracy improvement in cases of magnetic field distortion, which derive from the continuous update of the correction matrix **E**. This allowed us to keep an updated estimate of non-linearity and metal disturbance, and to use the correction in a nearly linear neighborhood of the distortion. Feuerstein et al. (2007) proposed a similar correction method for EMTS non-linearity based on a calibration with an OTS, but no state space approach was adopted and line-of-sight occlusion was not taken into account. The experimental setup encompasses ARTtrack2 (Advanced Realtime Tracking GmbH, Germany) cameras as OTS, a 3D Guidance (Ascension Technology Corporation, USA), and a metal plate for magnetic field distortion: after the correction, translation errors ranged from 13.61 to 26.84 mm. As proved in Experiment #2, the SF algorithm showed significantly better results (RMSE ranging from 0.5 mm to 3.5, depending on occlusion length), achieving a tracking accuracy up to ten times higher than the estimated static accuracy of the EMTS in the disturbed environment (RMSE 18.64 mm); it is comparable with the vendor's stated accuracy in a metal free environment (RMSE 1.6 mm). Furthermore, the acquisition was carried out in the disturbed setup with a quality indicator higher than 2; in such conditions the vendor recommends to completely discard the data, which on the contrary, have been successfully used in the SF algorithm. The correction matrix **E** makes also the filter less dependent on calibration accuracy: the calibration matrix Y mainly affects the filter, whereas the X matrix can be thought of as included in the correction **E**. A comparison with the hybrid electromagnetic inertial tracking proposed by Ren et al. (2012) is not possible since no information is given about electromagnetic field distortion.

In conclusion, the presented algorithm improves the performance of typical surgical tracking systems in terms of robustness to line-of-sight occlusion (OTS) and localization errors due to electromagnetic disturbance (EMTS), resulting in a continuous and reliable data stream to be displayed on the navigation monitor to the surgeon.

Chapter 4

Conclusions

Modern ORs show an increasing and massive use of technologies in terms of different modality of sensors, navigation systems, surgical robots, surgical instrumentation, intra-operative imaging, and surgical informatics for workflow management and decision support systems. Despite the advancements in the aforementioned fields, there is a clear need for integration of technologies in order to overcome the lack of compatible and interchangeable equipment. According to many experts of the field, in fact, one of the main needs towards the OR of the future is the interoperability of devices: currently, most of them function as stand-alone systems and their use requires a great effort to the surgeons (Cleary et al., 2005a).

The management of different sensors in the OR, as we already pointed out, has recently become an important part of modern CAS systems with particular reference to data synchronization. Correct timing of sensors data is crucial for the reliability of the information provided to the surgeon and thus for the safety of the procedure. Also, sensors data synchronization is a mandatory requirement to correctly combine information from different sources.

This need was recently received by a number of research efforts worldwide. Among them, the ROBOCAST project, funded by a EU grant (FP7-ICT-2007-215190), aimed at developing a modular system for robot-assisted minimally invasive neurosurgery. One of the main goals of the ROBOCAST project is the development of a comprehensive, modular and fully integrated system, which guides the surgeon from the pre-operative planning phase to the actual procedure in the OR. Part of the work presented in this thesis was carried out within the ROBOCAST project.

Chapter 4. Conclusions

Aim of this thesis, which was partially carried out within the ROBOCAST project, is to investigate methodologies for the management and integration of multimodal sensors in surgical applications and to study and develop a software framework for data acquisition and fusion.

Moreover, multi-sensor data fusion, which has been widely investigated in literature for applications to mobile robots control, autonomous vehicles, environment modeling and others, is an open research field with reference to surgical applications. Research efforts in this direction aim at overcoming the limitations of currently available tracking technologies for surgery, in order to ensure a more accurate and robust spatial localization of patient and surgical tools.

In Chapter 2, we proposed a centralized, multi-sensor management software architecture for a distributed CAS system. The software was developed as a data server module in a client–server architecture, using two open-source software libraries: IGSTK and OpenCV.

The advantages of a centralized management of multiple sensors were experimentally demonstrated. In particular the proposed architecture has two main scientific and technological implications:

- **Synchronization**. Ethernet communication can be adopted to reduce architecture complexity, avoiding traffic overhead of synchronous bus network. This is the case of the ROBOCAST architecture, where the communication bus does not carry synchronization information. In such conditions, we demonstrated that a unique time-stamping module for all the involved sensors limits the synchronization error to the accuracy of a single clock (typical quartz accuracy is 10 ÷ 100 ppm). The direct clinical implication of this is the safety of the procedure, which can be carried out on the basis of consistent information provided either to the surgeon or to the controller of a surgical robot.
- **Spatial alignment**. Complex CAS systems involve multiple Cartesian coordinate frames (e.g. pre-operative images, intra-operative images, localization systems, possible actuators), whose spatial relationships are often pre-computed with a calibration procedure. The centralized

module allows the pre-processing of the information coming from different sensors and intra-operative imaging device (e.g. US images) in order to provide the other modules with data correctly aligned in space: e.g. current instrument position is provided to the navigation display with respect to the image space, while the same information is transformed with respect to robot space before being transferred to the actuator controller.

The applicability of this architecture was successfully tested in the ROBOCAST final demonstrator showed at the Neurosurgery Department of the hospital *"Azienda Ospedaliera Universitaria Integrata Verona"* in Verona, Italy. The system was set up in a real OR and phantom experiments were successfully carried out.

As described in Chapter 3, the sensors management framework was then exploited and used as starting point to investigate multiple sensors fusion algorithms, with the target application of improving the performances of OTS and EMTS in terms of robustness to line-of-sight occlusion and electromagnetic field disturbances respectively. In crowded ORs it is often difficult to ensure clear visibility of all optically tracked objects, resulting in a discontinuous stream of localization data to be transferred to other modules of a CAS platform (e.g. navigation display). EMTSs do not have this flaw but provide less accurate measurements, particularly in presence of electromagnetic field distortion (e.g. metal objects or electrically powered devices, which are common in the OR). In such conditions, the degradation of EMTS accuracy can be as high as few centimeters, which is incompatible with the accuracy required by demanding stereotactic neurosurgical procedures (< 1mm).

To the best of our knowledge the proposed sensors fusion algorithm represents the first case in which OTS and EMTS were fused together with a probabilistic approach based on the Unscented Kalman filter. The proposed algorithm exploit EMTS data to compensate for optical line-of-sight occlusions whereas it continuously updates an error matrix **E,** representing the effects of electromagnetic field distortions, as long as the optical measurements are available (see Chapter 3): in this way when EMTS data are

needed, the correction is applied in a nearly linear neighborhood of the distortion. The clinical impact of the proposed solution was experimentally demonstrated, resulting in a continuous and reliable data stream to be displayed on the navigation monitor to the surgeon.

The proposed solution to the optical line-of-sight problem represents the main scientific outcome of this work not only for enhancing current state of the art navigation systems, but also in the vision of the OR of the future, already envisaged in some research projects all over the world (e.g. the "smartOR" project funded by the Federal Ministry of Economics and Technology of Germany; "OR of the future" at the Massachusetts General Hospital, Boston, MA, USA, and the "Medical Device Plug n Play" program directly evolved from the previous and involving a number of institutions in the U.S.). The research trend in this field is oriented to smart environments capable of observing understanding human-human and human-machine interactions, with the goal of a workflow control system able to react and adapt to current (or possibly future) situations, instead of simply being a rigid list of steps to be followed. Such context-aware systems must be equipped with a number of sensors (e.g. cameras, microphones, tracking systems etc.) to extract information on the operating theatre and human intentions and to react providing proactive services in terms of user-interface and workflow adaptation. As Bass (2000) pointed out, decision-support systems for situation awareness are tightly coupled with fusion systems. In this sense the proposed architecture is a step towards the new concept of an OR with a seamless interaction between surgeons and an intelligent assistive system, which detaches from rigid application interfaces and begins to approach the user by supporting the recognized intention.

In a more immediate timeframe, future developments of the presented work have two main directions: a) technological transfer and exploitation of the sensors management and fusion architecture and b) the extension of the framework to other sensing technology such as IMUs.

As regards industrial exploitation of the presented results, two more steps are needed. The first step is to study a particular CAS procedure and to intra-operatively acquire data about the surgical workflow and the entity of line-

of-sight occlusion in the specific setup of a real OR, so that the filter can be tailored and optimized for the particular application, in terms of parameters tuning and noise covariance estimation. This will be carried out in the near future thanks to a recently established collaboration between our laboratory (NearLab, Politecnico di Milano), the Neurosurgery department of the Niguarda Hospital (Milan, Italy) and Medtronic (Minneapolis, MN, USA) one of the main developers of surgical navigation suites, which will open its system to us for research purpose. The second step is to make the algorithm running on-line during the surgical procedure. To this extent, the sensor fusion algorithm will be implemented as a C++ module to be integrated with the SM.

The other direction for further development points towards the extension of the fusion algorithm to OTS and IMU. In fact, despite the good results of fusing together optical and electromagnetic localization data, hardware limitations of these tracking technologies do not allow having high update rate as required by robot control loop in complex surgical tasks. An example of such complexity can be found in the ACTIVE project, funded by EU grant FP7-ICT-2009-6-270460, which aims at developing a multi-robot system for patient-awake neurosurgery (e.g. epilepsy surgery). In the ACTIVE scenario, sudden and unpredictable patient motion must be detected or possibly anticipated in order for the robots to compensate the motion and to promptly react to safety critical conditions (e.g. epileptic seizure while the tool is in contact with the brain). Enhancing standard tracking techniques (e.g. optical tracking) with inertial measurements is therefore needed. Fusing together OTS and IMU on the one hand will again ensure robustness to line-of-sight occlusions and on the other will increase the update rate of the surgical tool pose estimation and provide information of where the tool is likely to be in the next time instants. IMUs are, in fact, capable of higher update rate (hundreds of Hz, compared to tens of Hz of OTS and EMTS) and provide information about linear acceleration and angular velocity that can help in predicting the tracked object motion.

Appendix A

Orientation representation

The orientation (or attitude) of a rigid body with respect to a fixed inertial coordinate system (*world coordinate system*) is expressed by the rotation to be applied to a body-fixed coordinate system (*local coordinate system*) to make it coincide with the world coordinate system. Different mathematical constructs allow the representation of a rigid body attitude in the three-dimensional space. This Appendix covers Euler angles, rotation matrices, unit quaternions and rotation vectors and the conversion between them.

A.1. Euler Angles

The most intuitive way to represent a rotation in the 3D space is to decompose it in three consecutive rotations about the coordinate axes. The values of these three rotations are called Euler Angles. Since rotation is non-commutative there are 27 possible sequence of rotation around the three axes (e.g. x-y-z, x-z-x, etc.): however only 12 of them satisfy the constraint that no two consecutive rotation axes in a valid sequence may be equal. Also, it must be specified whether the consecutive rotations are performed around the moving axes (intrinsic convention) or around the fixed axes (extrinsic convention).

We will focus on two commonly used sequences, z-x-z and x-y-z and the problem of singularities, which occur when the middle rotation aligns the axes of the first and last rotations.

A.1.1. Z-X-Z sequence

In this convention, the Euler angles, ϕ, θ, ψ, are known respectively as spin, nutation and precession. A commonplace example of gyroscopic motion is a spinning top. In this case, the body-fixed z-axis is aligned with the spin-

axis of the top, and the body-fixed x- and y-axes point out the sides of the top. The tilt of the top away from the world z-axis is the nutation angle, and the moment arising from this tilt produces the familiar slow orbiting motion, called precession.

This parameterization has singularities at nutation values of $\theta = n\pi$ for $n \in Z$. At these points, changes in spin and precession represent the same rotation.

It is a notable characteristic of this parameterization, and all parameterizations of the form (i; j; i), that there exists a singularity at the home position, $[\phi, \theta, \psi] = [0, 0, 0]$.

A.1.2. X-Y-Z sequence

The angles associated with this sequence are sometimes called Cardan angles. They are commonly used in computer graphics and aerospace engineering. These angles are also commonly referred to simply as Euler angles in the aeronautics field, in which ϕ, θ and ψ are known respectively as roll, pitch, and yaw, or, equivalently, bank, attitude, and heading.

This parameterization has singularities at pitch values of $\theta = \pi/2 + n\pi$, for $n \in Z$. It is thus only suitable for describing moving objects that do not perform vertical or inverted maneuvers, such as land vehicles, boats and transport aircrafts. All Euler angle sequences that do not have a repeated axis of rotation have this singularity.

A.2. Rotation Matrices

An orthogonal matrix whose determinant equals 1 can be used to perform a rotation in Euclidean space. The set of such matrices is the special orthogonal group denoted by SO(3).

We refer to the elements of a rotation matrix as follows:

$$\boldsymbol{R} = \begin{bmatrix} \boldsymbol{r}_1 & \boldsymbol{r}_2 & \boldsymbol{r}_3 \end{bmatrix} = \begin{bmatrix} r_{11} & r_{12} & r_{13} \\ r_{21} & r_{22} & r_{23} \\ r_{31} & r_{32} & r_{33} \end{bmatrix} \qquad \text{(a.1)}$$

Appendix A. Rotation representations

Given a vector **x**, expressed in world coordinate system and a rotation matrix, **R**, describing the attitude of a body-fixed coordinate system with respect to the world coordinate system, the following equations hold:

$$\begin{aligned} \boldsymbol{x}' &= \boldsymbol{R} \cdot \boldsymbol{x} \\ \boldsymbol{x} &= \boldsymbol{R}^T \cdot \boldsymbol{x}' \end{aligned} \tag{a.2}$$

being **x'** the same vector of **x** expressed in the body-fixed coordinate system.

The matrix **R** may also be referred to as direction cosine matrix, because its elements are the cosines of the unsigned angles between the body-fixed axes and the world axes.

Another interpretation of the matrix **R** is to consider it as the matrix of basis vectors that define the world and body-fixed coordinate systems. The rows of the rotation matrix are the basis vectors of the body-fixed coordinates expressed in world coordinates, and the columns are the basis vectors of the world coordinates expressed in the body-fixed coordinates.

Elementary rotations of an angle θ about the x-, y-, or z-axis, in three dimensions, are expressed by the following:

$$\boldsymbol{R}_x(\theta) = \begin{bmatrix} 1 & 0 & 0 \\ 0 & \cos\theta & -\sin\theta \\ 0 & \sin\theta & \cos\theta \end{bmatrix} \tag{a.3}$$

$$\boldsymbol{R}_y(\theta) = \begin{bmatrix} \cos\theta & 0 & -\sin\theta \\ 0 & 1 & 0 \\ \sin\theta & 0 & \cos\theta \end{bmatrix} \tag{a.4}$$

$$\boldsymbol{R}_z(\theta) = \begin{bmatrix} \cos\theta & -\sin\theta & 0 \\ \sin\theta & \cos\theta & 0 \\ 0 & 0 & 1 \end{bmatrix} \tag{a.5}$$

Appendix A. Rotation representations

A.3. Quaternions

The quaternions are a number system that extends the complex numbers, which find application to mechanics in three-dimensional space.

A quaternion is a linear combination expressed in the base {i,j,k}:

$$\boldsymbol{q} = q_0 1 + q_1 \boldsymbol{i} + q_2 \boldsymbol{j} + q_3 \boldsymbol{k} \tag{a.6}$$

where the coefficient q_0, q_1, q_2, q_3 are real.

In analogy with complex numbers, that are the sum of a real part and an imaginary part, quaternions can be considered as the sum of a real part q_0 and a vector part $\mathbf{q_v}$

$$\boldsymbol{q} = q_0 + \boldsymbol{q}_v = q_0 + \begin{bmatrix} q_1 \boldsymbol{i} & q_2 \boldsymbol{j} & q_3 \boldsymbol{k} \end{bmatrix} \tag{a.7}$$

Conjugate, norm and inverse of a quaternion are defined as follows:

$$\boldsymbol{q}^* = q_0 - \boldsymbol{q}_v \tag{a.8}$$

$$\|\boldsymbol{q}\| = \sqrt{q_0^2 + q_1^2 + q_2^2 + q_3^2} \tag{a.9}$$

$$\boldsymbol{q}^{-1} = \frac{\boldsymbol{q}^*}{\|\boldsymbol{q}\|} \tag{a.10}$$

The set of *unit quaternions*, i.e. quaternions with unit norm, can be used to represent rotations in the 3D space. For a unit quaternion the inverse and the conjugate coincide:

$$\boldsymbol{q}^{-1} = \boldsymbol{q}^* \tag{a.11}$$

We assume that a unit quaternion is represented by a sum of two trigonometric functions:

$$\boldsymbol{q} = \cos\boldsymbol{\theta} + \boldsymbol{u}\sin\boldsymbol{\theta} = \left(\cos\boldsymbol{\theta},\ \boldsymbol{u}\sin\boldsymbol{\theta}\right) \qquad \text{(a.12)}$$

where **u** is a unit norm vector and θ a generic angle.

Under this assumption, a quaternion **q** represents a rotation around **u** of an angle equals to 2θ.

Compared to Euler angles they are simpler to compose and avoid the problem of singularities, but present a sign ambiguity since **q** and **−q** represent the same rotation. Compared to rotation matrices they are more numerically stable and may be more efficient.

A.4. Rotation vectors

Euler's rotation theorem states that, in three-dimensional space, any displacement of a rigid body such that a point on the rigid body remains fixed, is equivalent to a single rotation about some axis that runs through the fixed point (see Fig. A1)

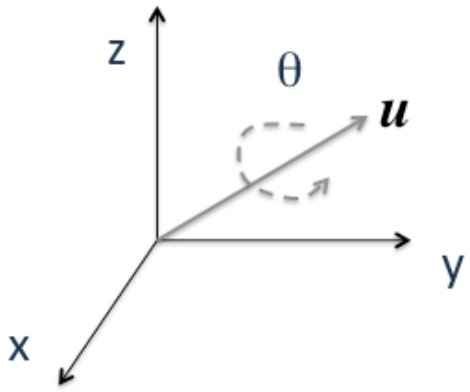

Fig. A1 - A rotation represented by an Euler axis (the unit vector u) and an angle θ

The extension of the theorem to kinematics yields the concept of instant axis of rotation. There are two ways to represent it:

- as a pair consisting of the angle and a unit vector for the axis, or
- as a vector obtained by multiplying the angle with this unit vector, called the *rotation vector*.

In this case, both the axis and the angle are represented by a non-normalized vector, **r**, co-directional with the axis **u** whose magnitude is the rotation angle, θ.

$$w = \begin{bmatrix} w^{p} & w^{v} & w^{\alpha,\beta,\gamma} & w^{\omega} \end{bmatrix}^{T} \tag{a.13}$$

A.5. Conversions

A.5.1. Euler Angles <--> Rotation Matrices

The orthogonal matrix corresponding to a rotation with Euler angles ϕ, θ, ψ, with x-y-z extrinsic (fixed axes) convention, is given by:

$$\begin{aligned} &\boldsymbol{R} = \boldsymbol{R}_z(\phi)\cdot\boldsymbol{R}_y(\theta)\cdot\boldsymbol{R}_x(\psi) = \\ &= \begin{bmatrix} \cos\phi\cos\theta & \cos\phi\sin\theta\sin\psi - \sin\phi\cos\psi & \cos\phi\sin\theta\cos\psi + \sin\phi\sin\psi \\ \sin\phi\cos\theta & \sin\phi\sin\theta\sin\psi + \cos\phi\cos\psi & \sin\phi\sin\theta\cos\psi - \cos\phi\sin\psi \\ -\sin\theta & \cos\theta\sin\psi & \cos\theta\cos\psi \end{bmatrix} \end{aligned} \tag{a.14}$$

To represent the same rotation with the intrinsic convention (moving axes), it is necessary to invert the order of matrix multiplication:

$$\boldsymbol{R} = \boldsymbol{R}_x(\phi)\cdot\boldsymbol{R}_y(\theta)\cdot\boldsymbol{R}_z(\psi) \tag{a.15}$$

Considering equation (a14), the three angles can be retrieved as follows:

$$\theta = \arctan 2\left(-r_{31},\ \pm\sqrt{r_{32}^2 + r_{33}^2}\right) \tag{a.16}$$

$$\psi = \arctan 2\left(\frac{r_{32}}{\cos\theta},\ \frac{r_{33}}{\cos\theta}\right) \tag{a.17}$$

$$\phi = \arctan 2\left(\frac{r_{21}}{\cos\theta},\ \frac{r_{11}}{\cos\theta}\right) \tag{a.18}$$

Where arctan2 is a variation of the standard arctan function with output on all four quadrants and defined as follows:

$$\arctan 2(y,\ x)=\begin{cases}\arctan\left(\frac{y}{x}\right), & x>0\\ \arctan\left(\frac{y}{x}\right)+\pi, & y\geq 0,\ x<0\\ \arctan\left(\frac{y}{x}\right)-\pi, & y<0,\ x<0\\ +\frac{\pi}{2} & y>0,\ x=0\\ -\frac{\pi}{2} & y<0,\ x=0\\ \text{undefined} & y=0,\ x=0\end{cases} \tag{a.19}$$

A.5.2. Euler Angles <--> Quaternions

The quaternion corresponding to a rotation with Euler angles ϕ, θ, ψ, with x-y-z extrinsic (fixed axes) convention, is given by:

$$\begin{cases} q_0 = -\cos\left(\frac{\phi-\psi}{2}\right)\sin\left(\frac{\theta}{2}\right)\\ q_1 = -\sin\left(\frac{\phi-\psi}{2}\right)\sin\left(\frac{\theta}{2}\right)\\ q_2 = -\sin\left(\frac{\phi+\psi}{2}\right)\cos\left(\frac{\theta}{2}\right)\\ q_3 = \sin\left(\frac{\phi+\psi}{2}\right)\cos\left(\frac{\theta}{2}\right)\end{cases} \tag{a.20}$$

The following equations allow the conversion from the quaternion $\boldsymbol{q}$ to the three angles ϕ, θ, ψ:

$$\begin{aligned}\boldsymbol{\phi} &= \arctan\left(\left(q_0 q_2 + q_1 q_3\right),\ \left(q_1 q_2 - q_0 q_3\right)\right)\\ \boldsymbol{\theta} &= \arccos\left(-q_0^2 - q_1^2 + q_2^2 + q_3^2\right)\\ \boldsymbol{\psi} &= -\arctan\left(\left(q_0 q_2 - q_1 q_3\right),\ \left(q_1 q_2 + q_0 q_3\right)\right)\end{aligned} \tag{a.21}$$

A.5.3. Rotation vector <--> Quaternions

The axis $\boldsymbol{u}$ and the angle θ, defining the rotation vector $\boldsymbol{r}$ (according to equation (a13)), can be retrieved from the quaternion $\boldsymbol{q}$ as follows:

$$\begin{aligned}\boldsymbol{\theta} &= 2 \cdot \arccos\left(q_0\right)\\ \boldsymbol{u} &= \begin{cases} \boldsymbol{\theta} \cdot \dfrac{\boldsymbol{q}_v}{\left\|\boldsymbol{q}_v\right\|}, & \boldsymbol{\theta} \neq 0 \\ \left[0,\ 0,\ 0\right] & \boldsymbol{\theta} = 0 \end{cases}\end{aligned} \tag{a.22}$$

The quaternion $\boldsymbol{q}$ describing the same rotation of the rotation vector $\boldsymbol{r} = \boldsymbol{u}\theta$, is the following:

$$\begin{aligned}q_0 &= \cos\left(\frac{\boldsymbol{\theta}}{2}\right)\\ \boldsymbol{q}_v &= \boldsymbol{u} \cdot \sin\left(\frac{\boldsymbol{\theta}}{2}\right)\end{aligned} \tag{a.23}$$

The same results of equations (a.21) and (a.22) yield from the exponential/log map, which maps a rotation vector describing the axis and magnitude of a 3D rotation to the corresponding quaternion and vice versa as follows:

$$\boldsymbol{q} = \exp\left(\boldsymbol{r}\right) = \left[\cos\left(\frac{\boldsymbol{\theta}}{2}\right),\ \boldsymbol{u}\sin\left(\frac{\boldsymbol{\theta}}{2}\right)\right] \tag{a.24}$$

$$\boldsymbol{r} = \log\left(\boldsymbol{q}\right) = 2\arccos\left(q_0\right) \cdot \frac{\boldsymbol{q}_v}{\left\|\boldsymbol{q}_v\right\|} \tag{a.25}$$

A.5.4. Rotation vector <--> Rotation Matrices

It is possible to retrieve the rotation vector $\boldsymbol{r} = \boldsymbol{u}\theta$, given a rotation matrix $\boldsymbol{R}$, as follows:

$$\begin{aligned} \boldsymbol{\theta} &= \arccos\left(\frac{r_{11}+r_{22}+r_{33}-1}{2}\right) \\ \boldsymbol{u} &= \frac{1}{2\sin(\boldsymbol{\theta})}\begin{bmatrix} r_{32}-r_{23} \\ r_{13}-r_{31} \\ r_{21}-r_{12} \end{bmatrix}, \qquad \boldsymbol{\theta} \neq 0 + \boldsymbol{k\pi} \end{aligned} \tag{a.26}$$

Given the unit vector $\boldsymbol{u} = [u_x, u_y, u_z]$, the transformation from the rotation vector $\mathbf{r} = \mathbf{u}\theta$ to the rotation matrix $\boldsymbol{R}$ is:

$$\boldsymbol{R} = \begin{bmatrix} u_x^2(1-\cos\boldsymbol{\theta})+\cos\boldsymbol{\theta} & u_x u_y(1-\cos\boldsymbol{\theta})-u_z\sin\boldsymbol{\theta} & u_x u_z(1-\cos\boldsymbol{\theta})+u_y\sin\boldsymbol{\theta} \\ u_x u_y(1-\cos\boldsymbol{\theta})+u_z\sin\boldsymbol{\theta} & u_y^2(1-\cos\boldsymbol{\theta})+\cos\boldsymbol{\theta} & u_y u_z(1-\cos\boldsymbol{\theta})-u_x\sin\boldsymbol{\theta} \\ u_x u_z(1-\cos\boldsymbol{\theta})-u_y\sin\boldsymbol{\theta} & u_y u_z(1-\cos\boldsymbol{\theta})+u_x\sin\boldsymbol{\theta} & u_z^2(1-\cos\boldsymbol{\theta})+\cos\boldsymbol{\theta} \end{bmatrix} \tag{a.27}$$

A.5.5. Rotation matrices <--> Quaternions

The following equation shows a way to compute a quaternion $\boldsymbol{q}$ from a rotation matrix $\boldsymbol{R}$:

$$\begin{cases} q_0 = \dfrac{1}{2}\sqrt{1+r_{11}+r_{22}+r_{33}} \\ q_1 = \dfrac{1}{4q_0}(r_{32}-r_{23}) \\ q_2 = \dfrac{1}{4q_0}(r_{13}-r_{31}) \\ q_3 = \dfrac{1}{4q_0}(r_{21}-r_{12}) \end{cases} \tag{a.28}$$

The transformation from the quaternion $\boldsymbol{q}$ to the rotation matrix $\boldsymbol{R}$ is:

$$\boldsymbol{R} = \left(q_0^2 - \boldsymbol{q}_v^T \boldsymbol{q}_v\right)\boldsymbol{I} + 2\boldsymbol{q}_v\boldsymbol{q}_v^T + 2q_0\boldsymbol{Q}$$

$$\text{where } Q = \begin{bmatrix} 0 & -q_3 & q_2 \\ q_3 & 0 & -q_1 \\ -q_2 & q_1 & 0 \end{bmatrix} \tag{a.29}$$

A.5.6. Euler Angles <--> Rotation Vectors

There is no direct unambiguous conversion between Euler angles and rotation vectors. Such conversion can be achieved using one of the abovementioned conversions to be used as an intermediate step, e.g. from Euler angles to rotation matrix and from rotation matrix to rotation vector.

Bibliography

Abolhassani, N., Patel, R. & Moallem, M. 2007, "Needle insertion into soft tissue: A survey", *Medical engineering & physics,* vol. 29, no. 4, pp. 413-431.

Angrisani, L., D'Apuzzo, M. & Moriello, R.S.L. 2006, "Unscented transform: a powerful tool for measurement uncertainty evaluation", *Instrumentation and Measurement, IEEE Transactions on,* vol. 55, no. 3, pp. 737-743.

Barnett, G.H., Kormos, D.W., Steiner, C.P. & Weisenberger, J. 1993, "Intraoperative localization using an armless, frameless stereotactic wand", *Journal of neurosurgery,* vol. 78, no. 3, pp. 510-514.

Bar-Shalom, Y., Li, X.R., Kirubarajan, T. & Wiley, J. 2001, *Estimation with applications to tracking and navigation,* Wiley Online Library.

Bass, T. 2000, "Intrusion detection systems and multisensor data fusion", *Communications of the ACM,* vol. 43, no. 4, pp. 99-105.

Bäthis, H., Perlick, L., Tingart, M., Lüring, C., Zurakowski, D. & Grifka, J. 2004, "Alignment in total knee arthroplasty a comparison of computer-assisted surgery with the conventional technique", *Journal of Bone & Joint Surgery, British Volume,* vol. 86, no. 5, pp. 682-687.

Beasley, R.A. & Howe, R.D. 2009, "Increasing accuracy in image-guided robotic surgery through tip tracking and model-based flexion correction", *Robotics, IEEE Transactions on,* vol. 25, no. 2, pp. 292-302.

Beller, S., Hünerbein, M., Lange, T., Eulenstein, S., Gebauer, B. & Schlag, P. 2007, "Image-guided surgery of liver metastases by three-dimensional ultrasound-based optoelectronic navigation", *British journal of surgery,* vol. 94, no. 7, pp. 866-875.

Bercik, P., Schlageter, V., Mauro, M., Rawlinson, J., Kucera, P. & Armstrong, D. 2005, "Noninvasive verification of nasogastric tube placement using a magnet-tracking system: a pilot study in healthy subjects", *Journal of Parenteral and Enteral Nutrition,* vol. 29, no. 4, pp. 305-310.

Berkelman, P.J., Whitcomb, L.L., Taylor, R.H. & Jensen, P. 2003, "A miniature microsurgical instrument tip force sensor for enhanced force feedback during robot-assisted manipulation", *Robotics and Automation, IEEE Transactions on,* vol. 19, no. 5, pp. 917-921.

Bezet, O. & Cherfaoui, V. 2005, "Timestamping uncertainties in distributed data acquisition systems", *Instrumentation and Measurement Technology Conference, 2005. IMTC 2005. Proceedings of the IEEE*IEEE, , pp. 2142.

Blasch, E. & Plano, S. 2002, "JDL Level 5 fusion model: user refinement issues and applications in group tracking", *SPIE Aerosense*, pp. 270.

Bucholz, R.D. & Smith, K.R. 1993, "A comparison of sonic digitizers versus light emitting diode-based localization", *Interactive Image-Guided Neurosurgery,* , pp. 179-200.

Bibliography

Cerveri, P., Pedotti, A. & Ferrigno, G. 2003, "Robust recovery of human motion from video using Kalman filters and virtual humans", *Human movement science,* vol. 22, no. 3, pp. 377-404.

Chung, A.J., Edwards, P.J., Deligianni, F. & Yang, G.Z. 2004, "Freehand cocalibration of optical and electromagnetic trackers for navigated bronchoscopy", *LECTURE NOTES IN COMPUTER SCIENCE,* , pp. 320-328.

Clatz, O., Delingette, H., Talos, I.F., Golby, A.J., Kikinis, R., Jolesz, F.A., Ayache, N. & Warfield, S.K. 2005, "Robust nonrigid registration to capture brain shift from intraoperative MRI", *Medical Imaging, IEEE Transactions on,* vol. 24, no. 11, pp. 1417-1427.

Cleary, K., Kinsella, A. & Mun, S.K. 2005a, "OR 2020 workshop report: Operating room of the future", vol. 1281, pp. 832-838.

Cleary, K., Zhang, H., Glossop, N., Levy, E., Wood, B. & Banovac, F. 2005b, "Electromagnetic tracking for image-guided abdominal procedures: Overall system and technical issues", *Engineering in Medicine and Biology Society, 2005. IEEE-EMBS 2005. 27th Annual International Conference of the*IEEE, , pp. 6748.

Comparetti, M.D., De Momi, E., Vaccarella, A., Riechmann, M. & Ferrigno, G. 2011, "Optically tracked multi-robot system for keyhole neurosurgery", *Robotics and Automation (ICRA), 2011 IEEE International Conference on*IEEE, , pp. 661.

Correll, K., Barendt, N. & Branicky, M. 2005, "Design considerations for software only implementations of the IEEE 1588 precision time protocol", *Conference on IEEE 1588 Standard for a Precision Clock Synchronization Protocol for Networked Measurement and Control Systems*Citeseer, .

Dai, Y., Tian, J., Yan, G. & Zheng, H. 2010, "Real-time visualized freehand 3D ultrasound reconstruction based on GPU", *Information Technology in Biomedicine, IEEE Transactions on,* vol. 14, no. 6, pp. 1338-1345.

Das, M., Sauer, F., Schoepf, U.J., Khamene, A., Vogt, S.K., Schaller, S., Kikinis, R. & Silverman, S.G. 2006, "Augmented Reality Visualization for CT-guided Interventions: System Description, Feasibility, and Initial Evaluation in an Abdominal Phantom1", *Radiology,* vol. 240, no. 1, pp. 230-235.

De Lorenzo, D., Manganelli, R., Dyagilev, I., Formaglio, A., De Momi, E., Prattichizzo, D., Shoham, M. & Ferrigno, G. 2010, "Miniaturized rigid probe driver with haptic loop control for neurosurgical interventions", *Biomedical Robotics and Biomechatronics (BioRob), 2010 3rd IEEE RAS and EMBS International Conference on*IEEE, , pp. 522.

De Momi, E., Beretta, E. & Ferrigno, G. 2012, "Hip joint centre localisation with an unscented Kalman filter", .

De Momi, E., Cerveri, P., Gambaretto, E., Marchente, M., Effretti, O., Barbariga, S., Gini, G. & Ferrigno, G. 2008, "Robotic alignment of femoral cutting mask during total knee arthroplasty", *International Journal of Computer Assisted Radiology and Surgery,* vol. 3, no. 5, pp. 413-419.

De Momi, E. & Ferrigno, G. 2010, "Robotic and artificial intelligence for keyhole neurosurgery: the ROBOCAST project, a multi-modal autonomous path planner", *Proceedings of the Institution of Mechanical Engineers, Part H: Journal of Engineering in Medicine,* vol. 224, no. 5, pp. 715-727.

Bibliography

De Momi, E., Lopomo, N., Cerveri, P., Zaffagnini, S., Safran, M.R. & Ferrigno, G. 2009, "In-vitro experimental assessment of a new robust algorithm for hip joint centre estimation", *Journal of Biomechanics,* vol. 42, no. 8, pp. 989-995.

De Vito, L., Rapuano, S. & Tomaciello, L. 2008, "One-way delay measurement: State of the art", *Instrumentation and Measurement, IEEE Transactions on,* vol. 57, no. 12, pp. 2742-2750.

DiGioia, A.M., Jaramaz, B. & Picard, F. 2004, *Computer and robotic assisted hip and knee surgery,* Oxford University Press, USA.

Elmenreich, W. 2007, "A review on system architectures for sensor fusion applications", *Software Technologies for Embedded and Ubiquitous Systems,* , pp. 547-559.

Elmenreich, W. & Pitzek, S. 2001, "The time-triggered sensor fusion model", *Proceedings of the 5th IEEE International Conference on Intelligent Engineering Systems*, pp. 297.

Emmerich, W. 2000, "Software engineering and middleware: a roadmap", *Proceedings of the Conference on The future of Software engineering*ACM, , pp. 117.

Enquobahrie, A., Cheng, P., Gary, K., Ibanez, L., Gobbi, D., Lindseth, F., Yaniv, Z., Aylward, S., Jomier, J. & Cleary, K. 2007, "The image-guided surgery toolkit IGSTK: an open source C software toolkit", *Journal of Digital Imaging,*vol. 20, pp. 21-33.

Eugster, P.T., Felber, P.A., Guerraoui, R. & Kermarrec, A.M. 2003, "The many faces of publish/subscribe", *ACM Computing Surveys (CSUR),* vol. 35, no. 2, pp. 114-131.

Feuerstein, M., Reichl, T., Vogel, J., Schneider, A., Feussner, H. & Navab, N. 2007, "Magneto-optic tracking of a flexible laparoscopic ultrasound transducer for laparoscope augmentation", *Medical Image Computing and Computer-Assisted Intervention–MICCAI 2007,* , pp. 458-466.

Fioretti, S. 1996, "Signal processing in movement analysis (a state-space approach)", *Human movement science,* vol. 15, no. 3, pp. 389-410.

Frantz, D., Wiles, A., Leis, S. & Kirsch, S. 2003, "Accuracy assessment protocols for electromagnetic tracking systems", *Physics in Medicine and Biology,* vol. 48, pp. 2241.

Freysinger, W., Gunkel, A.R., Bale, R., Vogele, M., Kremser, C., Schon, G. & Thumfart, W.F. 1998, "Three-dimensional navigation in otorhinolaryngological surgery with the viewing wand", *The Annals of Otology, Rhinology, and Laryngology,* vol. 107, no. 11 Pt 1, pp. 953-958.

Friets, E.M., Strohbehn, J.W., Hatch, J.F. & Roberts, D.W. 1989, "A frameless stereotaxic operating microscope for neurosurgery", *Biomedical Engineering, IEEE Transactions on,* vol. 36, no. 6, pp. 608-617.

Fürtjes, T., Korff, A., Follmann, A., Benzenberg, J., Schmieder, K. & Radermacher, K. 2011, "Line of sight optimization for a hand-held tool for neurosurgery", *Proceedings of CARS Conference 2011*, pp. 190.

Grassia, F.S. 1998, "Practical parameterization of rotations using the exponential map", *Journal of graphics tools,* vol. 3, pp. 29-48.

Bibliography

Gronningsaeter, A., Kleven, A., Ommedal, S., Aarseth, T.E., Lie, T., Lindseth, F., Langø, T. & Unsgård, G. 2000, "SonoWand, an ultrasound-based neuronavigation system", *Neurosurgery,* vol. 47, no. 6, pp. 1373-1380.

Grunert, P., Darabi, K., Espinosa, J. & Filippi, R. 2003, "Computer-aided navigation in neurosurgery", *Neurosurgical review,* vol. 26, no. 2, pp. 73-99.

Gunkel, A.R., Freysinger, W. & Thumfart, W.F. 2009, "Computer-Assisted Surgery in the Frontal and Maxillary Sinus", *The Laryngoscope,* vol. 107, no. 5, pp. 631-633.

Guo, T., Finnis, K.W., Parrent, A.G. & Peters, T.M. 2006, "Visualization and navigation system development and application for stereotactic deep-brain neurosurgeries", *Computer aided surgery,* vol. 11, no. 5, pp. 231-239.

Haidegger, T., Xia, T. & Kazanzides, P. 2008, "Accuracy improvement of a neurosurgical robot system", *Biomedical Robotics and Biomechatronics, 2008. BioRob 2008. 2nd IEEE RAS & EMBS International Conference on*IEEE, , pp. 836.

Halvorsen, K., Söderström, T., Stokes, V. & Lanshammar, H. 2005, "Using an extended kalman filter for rigid body pose estimation", *Journal of Biomechanical Engineering,* vol. 127, pp. 475.

Hananouchi, T., Saito, M., Koyama, T., Hagio, K., Murase, T., Sugano, N. & Yoshikawa, H. 2009, "Tailor-made surgical guide based on rapid prototyping technique for cup insertion in total hip arthroplasty", *The International Journal of Medical Robotics and Computer Assisted Surgery,* vol. 5, no. 2, pp. 164-169.

Horn, B.K.P. 1987, "Closed-form solution of absolute orientation using unit quaternions", *Journal of the Optical Society of America A,* vol. 4, no. 4, pp. 629-642.

Horsley, V. & Clarke, R.H. 1908, "The structure and functions of the cerebellum examined by a new method.", *Brain,* vol. 31, no. 1, pp. 45-124.

Hounsfield, S.G.N. "Computerized transversal axial scanning (tomography). 1. Description of system", *Br J Radiolog,* vol. 46, no. 552, pp. 1016-1022.

Ibanez, L., Enquobahrie, A., Turek, M., Jomier, J., Avila, R., Cheng, P., Yaniv, Z., Lindseth, F., Gary, K. & Cleary, K. 2008, "IGSTK: Building High Quality Roads with Open Source Software", .

Ijaz, U.Z., Chung, S.I., Khambampati, A.K., Kim, K.Y. & Kim, S. 2008, "Electrical resistance imaging of a time-varying interface in stratified flows using an unscented Kalman filter", *Measurement Science and Technology,* vol. 19, pp. 065501.

Jacobs, M.C. & Livingston, M.A. 1997, "Managing latency in complex augmented reality systems", *Proceedings of the 1997 symposium on Interactive 3D graphics*ACM, , pp. 49.

Jassemi-Zargani, R. & Necsulescu, D. 2002, "Extended Kalman filter-based sensor fusion for operational space control of a robot arm", *Instrumentation and Measurement, IEEE Transactions on,* vol. 51, no. 6, pp. 1279-1282.

Jensen, F.V. 1996, *An introduction to Bayesian networks,* UCL press London.

Jetto, L., Longhi, S. & Venturini, G. 1999, "Development and experimental validation of an adaptive extended Kalman filter for the localization of mobile

robots", *Robotics and Automation, IEEE Transactions on,* vol. 15, no. 2, pp. 219-229.

Johnston, H., Hilts, M., Beckham, W. & Berthelet, E. 2008, "3D ultrasound for prostate localization in radiation therapy: A comparison with implanted fiducial markers", *Medical physics,* vol. 35, pp. 2403.

Joskowicz, L. & Taylor, R.H. 2001, "Computers in imaging and guided surgery", *Computing in Science & Engineering,* vol. 3, no. 5, pp. 65-72.

Julier, S.J. 2002, "The scaled unscented transformation", *American Control Conference, 2002. Proceedings of the 2002*IEEE, , pp. 4555.

Julier, S.J. & Uhlmann, J.K. 2004, "Unscented filtering and nonlinear estimation", *Proceedings of the IEEE,* vol. 92, no. 3, pp. 401-422.

Kaempchen, N. & Dietmayer, K. 2003, "Data synchronization strategies for multi-sensor fusion", *Proceedings of the IEEE Conference on Intelligent Transportation Systems*Citeseer, .

Kais, M., Millescamps, D., Bétaille, D., Lusetti, B. & Chapelon, A. 2006, "A multi-sensor acquisition architecture and real-time reference for sensor and fusion methods benchmarking", *Intelligent Vehicles Symposium, 2006 IEEE*IEEE, , pp. 418.

Kirsch, S. 2005, "Accuracy assessment of the electromagnetic tracking system aurora", *Northern Digital white paper,* .

Klimek, L., Ecke, U., Lübben, B., Witte, J. & Mann, W. 2009, "A Passive-Marker-Based Optical System for Computer-Aided Surgery in Otorhinolaryngology: Development and First Clinical Experiences", *The Laryngoscope,* vol. 109, no. 9, pp. 1509-1515.

Ko, S., Frasson, L. & Rodriguez y Baena, F. 2011, "Closed-Loop Planar Motion Control of a Steerable Probe With a 'Programmable Bevel' Inspired by Nature", *Robotics, IEEE Transactions on,* , no. 99, pp. 1-14.

Kopetz, H. & Bauer, G. 2003, "The time-triggered architecture", *Proceedings of the IEEE,* vol. 91, no. 1, pp. 112-126.

Kraft, E. 2003, "A quaternion-based unscented kalman filter for orientation tracking", *Proceedings of the Sixth International Conference of Information Fusion*, pp. 47–54.

Krücker, J., Xu, S., Glossop, N., Viswanathan, A., Borgert, J., Schulz, H. & Wood, B.J. 2007, "Electromagnetic tracking for thermal ablation and biopsy guidance: clinical evaluation of spatial accuracy", *Journal of Vascular and Interventional Radiology,* vol. 18, no. 9, pp. 1141-1150.

Kuipers, J.B. 1980, "SPASYN-an electromagnetic relative position and orientation tracking system", *Instrumentation and Measurement, IEEE Transactions on,* vol. 29, no. 4, pp. 462-466.

Lange, T., Eulenstein, S., Hünerbein, M., Lamecker, H. & Schlag, P.M. 2004, "Augmenting intraoperative 3D ultrasound with preoperative models for navigation in liver surgery", *Medical Image Computing and Computer-Assisted Intervention–MICCAI 2004,* , pp. 534-541.

Leksell, L. 1951, "The stereotaxic method and radiosurgery of the brain", *Acta Chirurgica Scandinavica,* vol. 102, no. 4, pp. 316-319.

Bibliography

Lindseth, F., Kaspersen, J.H., Ommedal, S., Langø, T., Bang, J., Hokland, J., Unsgaard, G. & Nagelhus Hemes, T.A. 2003, "Multimodal image fusion in ultrasound-based neuronavigation: improving overview and interpretation by integrating preoperative MRI with intraoperative 3D ultrasound", *Computer Aided Surgery,* vol. 8, no. 2, pp. 49-69.

Luo, R.C., Yih, C.C. & Su, K.L. 2002, "Multisensor fusion and integration: approaches, applications, and future research directions", *Sensors Journal, IEEE,* vol. 2, no. 2, pp. 107-119.

Mirota, D.J., Hager, G.D. & Ishii, M. 2011, "Vision-Based Navigation in Image-Guided Interventions", *Annual Review of Biomedical Engineering,* vol. 13.

Mönnich, H., Botturi, D., Raczkowsky, J. & Wörn, H. 2009, "System Architecture for Workflow Controlled Robotic Surgery", *The Journal on Information Technology in Healthcare,* , pp. 345.

Mozer, P., Leroy, A., Payan, Y., Troccaz, J., Chartier-Kastler, E. & Richard, F. 2005, "Computer-assisted access to the kidney", *The International Journal of Medical Robotics and Computer Assisted Surgery,* vol. 1, no. 4, pp. 58-66.

Na, C., Obradovic, D., Scheiterer, R.L., Steindl, G. & Goetz, F.J. 2007, "Synchronization performance of the precision time protocol", *Precision Clock Synchronization for Measurement, Control and Communication, 2007. ISPCS 2007. IEEE International Symposium on*IEEE, , pp. 25.

Nafis, C., Jensen, V., Beauregard, L. & Anderson, P. 2006, "Method for estimating dynamic EM tracking accuracy of surgical navigation tools", *Medical Imaging,* , pp. 61410K-16.

Nijmeh, A., Goodger, N., Hawkes, D., Edwards, P. & McGurk, M. 2005, "Image-guided navigation in oral and maxillofacial surgery", *British Journal of Oral and Maxillofacial Surgery,* vol. 43, no. 4, pp. 294-302.

Ohue, S., Kumon, Y., Nagato, S., Kohno, S., Harada, H., Nakagawa, K., Kikuchi, K., Miki, H. & Ohnishi, T. 2010, "Evaluation of Intraoperative Brain Shift Using an Ultrasound-Linked Navigation System for Brain Tumor Surgery",*Neurologia medico-chirurgica,* vol. 50, no. 4, pp. 291-300.

Park, S., Aglyamov, S., Scott, W.G. & Emelianov, S. 2006, "Elasticity imaging using high frame rate ultrasound imaging", *Proceedings of the 2006 IEEE Ultrasonics Symposium (in print)*.

Peters, H., Raczkowsky, J. & Woern, H. 2005, "Approach to an architecture for a generic computer integrated surgery system", *Intelligent Robots and Systems, 2005. (IROS 2005). 2005 IEEE/RSJ International Conference on*IEEE, , pp. 2455.

Puangmali, P., Althoefer, K. & Seneviratne, L.D. 2010, "Mathematical modeling of intensity-modulated bent-tip optical fiber displacement sensors", *Instrumentation and Measurement, IEEE Transactions on,* vol. 59, no. 2, pp. 283-291.

Puangmali, P., Althoefer, K., Seneviratne, L.D., Murphy, D. & Dasgupta, P. 2008, "State-of-the-art in force and tactile sensing for minimally invasive surgery", *Sensors Journal, IEEE,* vol. 8, no. 4, pp. 371-381.

Rao, R.P.N. 1999, "An optimal estimation approach to visual perception and learning", *Vision research,* vol. 39, no. 11, pp. 1963-1989.

Bibliography

Reinhardt, H. & Zweifel, H.J. 1990, "Interactive sonar-operated device for stereotactic and open surgery", *Stereotactic and functional neurosurgery,* vol. 54, no. 1-8, pp. 393-397.

Reintsema, D., Preusche, C., Ortmaier, T. & Hirzinger, G. 2004, "Toward High-Fidelity Telepresence in Space and Surgery Robotics", *Presence: Teleoperators and Virtual Environments,* vol. 13, no. 1, pp. 77-98.

Ren, H., Rank, D., Merdes, M., Stallkamp, J. & Kazanzides, P. 2012, "Multisensor data fusion in an integrated tracking system for endoscopic surgery", *IEEE transactions on information technology in biomedicine : a publication of the IEEE Engineering in Medicine and Biology Society,* vol. 16, no. 1, pp. 106-111.

Ren, H., Rank, D., Merdes, M., Stallkamp, J. & Kazanzides, P. 2011, "Development of a wireless hybrid navigation system for laparoscopic surgery", *Studies in health technology and informatics,* vol. 163, pp. 479-485.

Roberts, D.W., Strohbehn, J.W., Hatch, J.F., Murray, W. & Kettenberger, H. 1986, "A frameless stereotaxic integration of computerized tomographic imaging and the operating microscope", *Journal of neurosurgery,* vol. 65, no. 4, pp. 545-549.

Roetenberg, D., Slycke, P.J. & Veltink, P.H. 2007, "Ambulatory position and orientation tracking fusing magnetic and inertial sensing", *Biomedical Engineering, IEEE Transactions on,* vol. 54, no. 5, pp. 883-890.

Rossi, A., Trevisani, A. & Zanotto, V. 2005, "A telerobotic haptic system for minimally invasive stereotactic neurosurgery", *The International Journal of Medical Robotics and Computer Assisted Surgery,* vol. 1, no. 2, pp. 64-75.

Schmidt, T. 2010, "Robotics: Environmental Awareness Through Cognitive Sensor Fusion", *Order,* vol. 501, pp. 2981.

Schwald, B. & Seibert, H. 2004, "Registration tasks for a hybrid tracking system for medical augmented reality", *Journal of WSCG,* vol. 12, pp. 411-418.

Seyler, T.M., Lai, L.P., Sprinkle, D.I., Ward, W.G. & Jinnah, R.H. 2008, "Does computer-assisted surgery improve accuracy and decrease the learning curve in hip resurfacing? A radiographic analysis", *The Journal of Bone & Joint Surgery,* vol. 90, no. Supplement_3, pp. 71-80.

Simpson, A.L., Ma, B., Chen, E.C.S., Ellis, R.E. & Stewart, A.J. 2007, "Computation and Validation of Intra-operative Camera Uncertainty", *Engineering in Medicine and Biology Society, 2007. EMBS 2007. 29th Annual International Conference of the IEEE*IEEE, , pp. 479.

Spiegel, E., Wycis, H., Marks, M. & Lee, A. 1947, "Stereotactic apparatus for operations", *Science,* vol. 106, pp. 439-450.

Strauss, G., Limpert, E., Strauss, M., Hofer, M., Dittrich, E., Nowatschin, S. & Luth, T. 2009, "Evaluation of a daily used navigation system for FESS]", *Laryngo- rhino-otologie,* vol. 88, no. 12, pp. 776-781.

Sugano, N. 2003, "Computer-assisted orthopedic surgery", *Journal of orthopaedic science,* vol. 8, no. 3, pp. 442-448.

Sun, S.L. & Deng, Z.L. 2004, "Multi-sensor optimal information fusion Kalman filter", *Automatica,* vol. 40, no. 6, pp. 1017-1023.

Bibliography

Talairach, J. 1957, *Atlas d'anatomie stéréotaxique: repérage radiologique indirect des noyaux gris centraux des régions mésencéphalo-sous-optique et hypothalamique de l'homme,* Masson.

Tan, U., Yang, B., Gullapalli, R. & Desai, J.P. 2011, "Triaxial MRI-Compatible Fiber-optic Force Sensor", *Robotics, IEEE Transactions on,* vol. 27, no. 1, pp. 65-74.

Tanaka, K., Hori, K., Kuroda, T. & Mitsuishi, M. 2004, "Integrated Control of Tele-surgery Robot System using CORBA Middleware", *Japan Journal of Medical Informatics,* vol. 24, no. 1, pp. 45-53.

Tanaka, Y., Nariai, T., Momose, T., Aoyagi, M., Maehara, T., Tomori, T., Yoshino, Y., Nagaoka, T., Ishiwata, K. & Ishii, K. 2009, "Glioma surgery using a multimodal navigation system with integrated metabolic images", *Journal of neurosurgery,* vol. 110, no. 1, pp. 163-172.

Taylor, R.H. & Kazanzides, P. 2008, "Medical Robotics and Computer-Integrated Interventional Medicine*", *Advances in Computers,* vol. 73, pp. 219-260.

Taylor, R.H. & Stoianovici, D. 2003, "Medical robotics in computer-integrated surgery", *Robotics and Automation, IEEE Transactions on,* vol. 19, no. 5, pp. 765-781.

Tobergte, A., Pomarlan, M. & Hirzinger, G. 2009, "Robust multi sensor pose estimation for medical applications", *Intelligent Robots and Systems, 2009. IROS 2009. IEEE/RSJ International Conference on*IEEE, , pp. 492.

Todd, E. 1967, "Todd-Wells Manual of Stereotaxic Procedures", *Randolph, Codman & Schurtleff,* .

Unsgård, G., Solheim, O., Lindseth, F. & Selbekk, T. 2011, "Intra-operative Imaging with 3D Ultrasound in Neurosurgery", *Intraoperative Imaging,* , pp. 181-186.

Vaccarella, A., Cerveri, P., De Momi, E. & Ferrigno, G. 2010, *A new IGSTK-based architecture for the integration of multimodal sensors and robots in neurosurgical robotics applications*, Geneve edn.

Vaccarella, A., De Momi, E., Valenti, M., Ferrigno, G. & Enquobahrie, A. 2012a, "Application of unscented Kalman filter for robust pose estimation in image-guided surgery", *Proceedings of SPIE*, pp. 83161K.

Vaccarella, A., Enquobahrie, A., Ferrigno, G. & Momi, E.D. 2012b, "Modular multiple sensors information management for computer-integrated surgery", *The International Journal of Medical Robotics and Computer Assisted Surgery,* .

Vaccarella, A., Khreis, G., Comparetti, M.D., Cappelletti, A., De Momi, E. & Ferrigno, G. 2011, "Data acquisition architecture for 3D ultrasound: temporal calibration", *Int J CARS,* vol. 6, no. 1, pp. S37-S38.

Van Der Merwe, R., Wan, E.A. & Julier, S. 2004, "Sigma-point Kalman filters for nonlinear estimation and sensor-fusion—Applications to integrated navigation", *Proceedings of the AIAA Guidance, Navigation & Control Conference*, pp. 16.

Varshney, P. 1997, "Multisensor data fusion", *Electronics & Communication Engineering Journal,* vol. 9, no. 6, pp. 245-253.

Bibliography

Willems, P.W.A., van der Sprenkel, J.W.B., Tulleken, C.A.F., Viergever, M.A. & Taphoorn, M.J.B. 2006, "Neuronavigation and surgery of intracerebral tumours", *Journal of neurology,* vol. 253, no. 9, pp. 1123-1136.

Willoughby, T.R., Kupelian, P.A., Pouliot, J., Shinohara, K., Aubin, M., Roach, M., Skrumeda, L.L., Balter, J.M., Litzenberg, D.W. & Hadley, S.W. 2006, "Target localization and real-time tracking using the Calypso 4D localization system in patients with localized prostate cancer", *International Journal of Radiation Oncology* Biology* Physics,* vol. 65, no. 2, pp. 528-534.

Wong, P., Muanza, T., Reynard, E., Robert, K., Barker, J. & Sultanem, K. 2011, "Use of three-dimensional ultrasound in the detection of breast tumor bed displacement during radiotherapy", *International Journal of Radiation Oncology* Biology* Physics,* vol. 79, no. 1, pp. 39-45.

Wood, B.J., Zhang, H., Durrani, A., Glossop, N., Ranjan, S., Lindisch, D., Levy, E., Banovac, F., Borgert, J. & Krueger, S. 2005, "Navigation with electromagnetic tracking for interventional radiology procedures: a feasibility study", *Journal of vascular and interventional radiology,* vol. 16, no. 4, pp. 493-505.

Wu, H., Siegel, M., Stiefelhagen, R. & Yang, J. 2002, "Sensor fusion using Dempster-Shafer theory [for context-aware HCI]", *Instrumentation and Measurement Technology Conference, 2002. IMTC/2002. Proceedings of the 19th IEEE*IEEE, , pp. 7.

Yang, H. & Zhang, J.Q. 2005, "An Unscented Kalm an Filter-Based MultisensorTrack Fusion Algorithm", *Instrumentation and Measurement Technology Conference, 2005. IMTC 2005. Proceedings of the IEEE*IEEE, , pp. 527.

Yaniv, Z., Cheng, P., Wilson, E., Popa, T., Lindisch, D., Campos-Nanez, E., Abeledo, H., Watson, V., Cleary, K. & Banovac, F. 2010, "Needle-based interventions with the image-guided surgery toolkit (IGSTK): From phantoms to clinical trials", *Biomedical Engineering, IEEE Transactions on,* vol. 57, no. 4, pp. 922-933.

Yoon, H.J., Zhao, K.D., Rebellato, J., An, K.N. & Keller, E.E. 2006, "Kinematic study of the mandible using an electromagnetic tracking device and custom dental appliance: Introducing a new technique", *Journal of Biomechanics,* vol. 39, no. 12, pp. 2325-2330.

You, S. & Neumann, U. 2001, "Fusion of vision and gyro tracking for robust augmented reality registration", *Virtual Reality, 2001. Proceedings. IEEE*IEEE, , pp. 71.

Zhang, H., Banovac, F., Lin, R., Glossop, N., Wood, B.J., Lindisch, D., Levy, E. & Cleary, K. 2006, "Electromagnetic tracking for abdominal interventions in computer aided surgery", *Computer Aided Surgery,* vol. 11, no. 3, pp. 127-136.

Zhang, L., Tamminedi, T., Ganguli, A., Yosiphon, G. & Yadegar, J. 2010, "Hierarchical multiple sensor fusion using structurally learned Bayesian network", *Wireless Health 2010*ACM, , pp. 174.

Zhou, H., Hu, H. & Tao, Y. 2006, "Inertial measurements of upper limb motion", *Medical and Biological Engineering and Computing,* vol. 44, no. 6, pp. 479-487.